

# THE IMPORTANCE OF SIZE AND SHAPE IN IMPRINTED POLYMERS

A Thesis

Submitted to the Graduate Faculty of the  
Louisiana State University and  
Agricultural and Mechanical College

In partial fulfillment of the  
requirements for the degree of  
Master of Science

in

The Department of Chemistry

by

Jason Campbell

B.S. Louisiana State University, Shreveport, 1998

December 2005

# Table of Contents

ABSTRACT.....	iii
CHAPTER	
1 INTRODUCTION.....	1
2 SYSTEMATIC STUDY OF STERIC AND SPATIAL CONTRIBUTIONS TO MOLECULAR RECOGNITION BY NON-COVALENT IMPRINT POLYMERS.....	6
3 OPTIMAL SPATIAL FIT AND SHAPE SELECTIVITY.....	16
4 STRUCTURAL CHANGES AND AGGREGATION OF HUMAN INFLUENZA VIRUS.....	32
REFERENCES.....	58
APPENDIX : LETTERS OF PERMISSION INFORMATION.....	62
VITA.....	65

## Abstract

The existence of shape selectivity in non-covalent molecularly imprinted polymers has been proven using molecular probes. A series of amines varying with different structural motifs and secondary amines with different sized side chains were imprinted, and binding evaluated by HPLC for each amine on polymers imprinted with similar amines. Trends in the binding relationships revealed two major contributions of cavity structure on selectivity afforded by molecularly imprinted polymers (MIPs). First, sterics play a dominant role in cases where a molecule's structure is too big to fit into an imprinted site formed from a smaller template molecule. Second, molecular structures that are equal to or smaller than those of the template molecule are selected by maximizing Van der Waals interactions within the MIP binding site.

# Chapter 1

## Introduction

## 1.1 Chiral Separation Methods in Chromatography

Chiral separations are commonly used in the pharmaceutical industry where obtaining an enantiomerically pure compound is often necessary. The enantiomers of chiral molecules can produce critically different pharmacological effects in biological systems. Current research in chiral separations explores the uses of a variety of chiral stationary phases (CSP) for use in liquid chromatography. Common techniques used are capillary electrophoresis, thin layer chromatography, subcritical and supercritical fluid chromatography, gas chromatography, and liquid chromatography.<sup>1</sup> Commercial chiral stationary phases for HPLC were first developed by William H. Pirkle.<sup>2</sup> Pirkle columns use chiral molecules covalently bonded to silica to separate enantiomers. Pirkle columns are able to separate a wide range of chiral compounds, durable, and allow the use of a wide range of solvents.

All chiral separation phases are governed by the three-point rule<sup>3</sup> which is restated by Pirkle that *Chiral recognition requires a minimum of three simultaneous interactions between the CSP and at least one of the enantiomers, with at least one of these interactions being stereochemically dependent.*<sup>2</sup> The three-point rule only requires that one of the forces be an attractive force and the others can be attractive forces or steric forces. The three-point rule is often misinterpreted or confused with the “three-point binding” theory that Ogsten proposed to explain the chiral binding selectivity of enzyme catalyzed reactions.<sup>4</sup> The three-point rule differs from the Ogsten’s model in that it requires only one interaction have an attractive force, while Ogsten’s model requires multiple attractive interactions.

## 1.2 Introduction to Molecularly Imprinted Polymers

Molecularly imprinted polymers (MIPs) were first developed by Wulff<sup>5</sup> as a mimic for enzymatic systems. Polymers with imprinted molecular recognition are easier to produce, less expensive, have greater stability, and are more chemically compatible with organic solvents than biological molecules. Furthermore, the ability to customize MIPs allows for increased binding specificity over systems such as silica gel, carbohydrates, or macroporous polymers; and they can be tailored to virtually any molecule.

Formation of MIPs involves using functional and cross-linking monomers in the presence of a target molecule that acts as a molecular template. The functional monomers form a complex with the target molecule using either covalent or non-covalent interactions prior to polymerization. The use of covalently bound target molecules was pioneered by Wulff,<sup>6</sup> while the non-covalent approach to imprinting was pioneered by Mosbach.<sup>7</sup> Once polymerized, the complex is postulated to be held into place by the cross-linking monomers. The template molecule can then be removed from the polymer leaving behind an imprinted site that is complementary in size, shape, and functionality to the target molecule. The polymer now has sites that are capable of recognizing and rebinding the target molecule with high specificity. A representation of molecular imprinting can be seen in figure 1. MIPs have been used for a variety of applications based on their recognition properties including chiral separations, sensors, and solid phase extraction materials. Research has also been done in an effort to use MIPs for catalysis.<sup>8</sup>

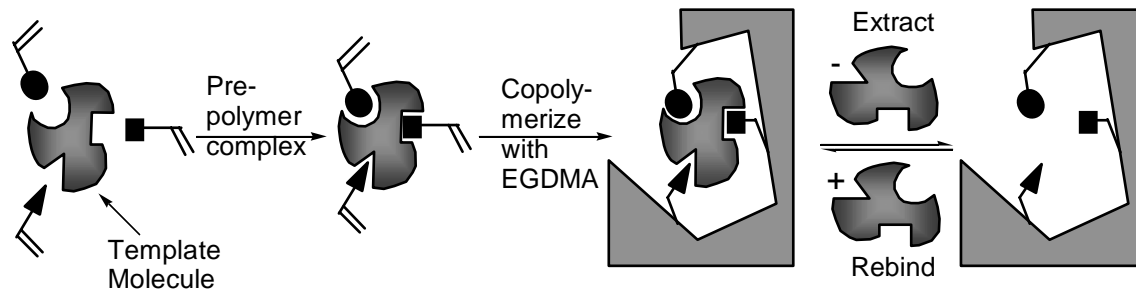


**Figure 1.1.** Formation of molecularly imprinted polymers.

One problem in implementing imprinted polymers instead of other separation supports in industrial applications is the affinity distribution of binding sites.<sup>9</sup> When a molecularly imprinted polymer is formed, it is with multiple interactions during polymerizations and without a great deal of fine control. The lack of fine control is in part due to the randomness of free radical polymerization leads to a binding affinity distribution of sites that are both specific (good sites) and non-specific at binding (bad sites).<sup>9</sup> The distribution of sites can lead to low average binding affinities or low average reaction rates for catalytic MIPs.<sup>8</sup> Another limitation is that MIPs are typically made as a bulk porous polymer, which means all binding is also governed by the different accessibility of sites throughout the polymer matrix. Some would be good sites go unused, because of slow mass transfer kinetics due to slow diffusion into and out of these sites in the polymer matrix.

It is the goal of this research to better understand some of the fundamentals of binding in molecularly imprinted polymers in order to be able to predict what type of molecules will make better targets for separations using MIPs. These experiments will be used to provide a better basic understanding of the binding in molecularly imprinted polymers and investigate the importance of the size and shape of the template molecule

on a MIP's performance with regard to specificity of molecular recognition. It will explore and better understand the influence of sterics on binding in MIPs. It has previously been shown that molecules can be separated based on their three dimensional shape,<sup>6</sup> but the degree to which sterics influences binding has never been systematically evaluated.

## Chapter 2

# Systematic Study of Steric and Spatial Contributions to Molecular Recognition by Non-Covalent Imprinted Polymers

## 2.1 Introduction

Non-covalent imprinting is the most widely used form of imprinting in polymers, because the polymers are easier to prepare and outperform covalently imprinted polymers. When a non-covalent imprinting system is used the target molecule must first self-assemble into a pre-polymer complex with one or more functional monomers. The polymerization of cross-linking monomer around the pre-polymer complex and removal of the target molecule leaves a cavity that is complimentary in size, shape, and functionality to the target molecule. Through binding studies it can be shown that the polymer then preferentially binds the target molecule over other molecules. The process of non-covalent molecular imprinting has been shown to be successful for the binding of variety of target molecules.<sup>10</sup> The effectiveness of an imprinted polymer is demonstrated by the binding of the target molecule and molecules with similar features. By studying molecules with similar features the cross-reactivity of the polymer can be assessed to quantify the selectivity of binding.<sup>11-14</sup>

These previous assessments a number of architectural elements have been shown to factor into to both the strength and selectivity of binding in MIPs, but the individual contribution of molecular interactions and their effects on selectivity and binding affinity have not been well established. A systematic study of binding would be helpful to better understand the binding of target molecules in non-covalent MIPs. Presented here is a study of enantioselectivity in MIPs using chiral substituted amines with a focus on the steric, distal, and conformational factors on the chiral selectivity of non-covalently MIPs. Enantiomers are best to use for probing cavity shape, because all the physical properties

for enantiomers are the same with the exception of the three dimensional positioning of the atoms in space. If the enantiomers have only one binding functionality, the change in three dimensional space should only alter the binding of the site due to increased steric interactions between a binding site made from the S enantiomer and the target molecule of the R enantiomer. As the sizes of different non-binding groups of the template increase the differences in binding affinity should also increase due to increased steric interactions.

In this study the template molecules employed have a single amine functionality that is used to form the pre-polymer complex and the primary rebinding interaction. Since the pre-polymer complex only has one type of binding group, then the only factors that should remain to give recognition are the steric differences between template and its enantiomer. It has been noted that the difficulty in creating cavities that are complementary in shape to small molecules may be due to the similar size of the monomer.<sup>15</sup> MIPs should not be expected to have a highly complimentary surface for small target molecules, but the resolution should increase with the size of the target molecule due to increased steric interactions.

## 2.2 Experimental

Ethylene glycol dimethacrylate (EGDMA, Polyscience) was distilled *in vacuo* (94°C) over boiling chips prior to polymerization. Methacrylic acid (MAA, Aldrich) was distilled over CaH<sub>2</sub> (80°C) prior to polymerization. R and S enantiomers of  $\alpha$ -methylbenzylamine,  $\beta$ -methylphenethylamine, 1-(1-naphthyl)ethylamine, bis ( $\alpha$  – methylbenzyl)amine, bis[(1-naphthyl)ethyl]amine, 1-aminoindane, and 2,2'-

azobisisobutyronitrile (AIBN) were purchased from Aldrich and used as received.

Solvents were obtained from commercial suppliers and purified prior to use.

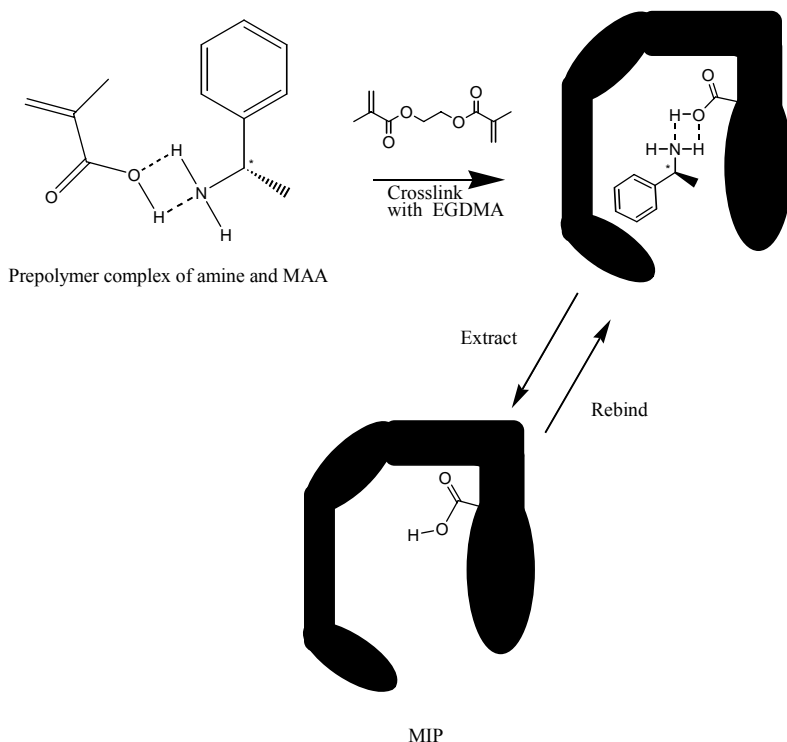


**Figure 2.1.** Molecular Imprinting model of the amine single point binding interaction used in this study.

All imprinted polymers were formed in 20 mL borosilicate glass scintillation vials. 1.28 mmol of the S enantiomer of the chiral amine was dissolved in 8.0 mL of methylene chloride. 5.0 g of EGDMA (25.2 mmol), 0.53 g MAA (6.3 mmol), and 0.11 g AIBN (0.64 mmol) were added. The solution was purged by bubbling nitrogen gas into the vial for 5 min before the vial was capped and sealed with teflon tape and parafilm. The samples were then inserted into a photochemical turntable reactor (ACE Glass Inc.) which was immersed in a constant temperature bath. A standard laboratory UV light source (a Canrad-Hanovia medium pressure 450W mercury arc lamp), jacketed in a

borosilicate double-walled immersion well, was placed at the center of the turntable. The polymerization was then initiated photochemically at 20°C and allowed to proceed for 10 h. The polymers were then washed with methanol by Soxhlet extraction and ground to a particle size between 20-25 µm with a mortar and pestle. The control polymers were made in a similar fashion without the addition of the amine.

For chromatographic experiments the polymer particles were slurry packed with excess acetonitrile into stainless steel columns (length, 10.0 cm; id, 4.6 mm) to full volume (approximately 60 mg of polymer) using a Beckman 1108 Solvent Delivery Module. Polymers were washed online for 12 h using acetonitrile-acetic acid (90:10) at a flow rate of 0.2 mL min<sup>-1</sup> to remove any leftover template. HPLC analyses were performed isocratically at room temperature using a Hitachi L-7100 pump with a Hitachi L-7400 UV detector. The flow rate was set to 1.0 mL min<sup>-1</sup> using a mobile phase of acetonitrile-acetic acid (90:10). Sample injections were 1.5-10 µL of a 10mM solution of amine in acetonitrile. The void volume of the column was determined with acetone. The separation factors ( $\alpha$ ) were measured as the ratio of capacity factors ( $k'_S/k'_R$ ). The capacity factors were determined by the relation of the retention volume and the void volume as follows  $k' = (R_v - D_v)/D_v$ .

### 2.3 Results and Discussion

The amine functionality was chosen for its reliable formation of a pre-polymer complex and rebinding.<sup>16</sup> This also gave a single common non-covalent binding interaction for each compound. This is important because the three-point rule for enantioselectivity requires three points of contact between the substrate and receptor.<sup>3</sup> This demands that enantioselectivity of polymers will be due to at least two other

interactions, and these interactions are steric in origin in the absence of any other interactions. All the template molecules were three dimensionally modeled in order to make comparisons before binding studies were done and appear in Table 2.1.

**Table 2.1.** Structure of chiral amines used for molecular imprinting, and space filling models illustrating the minimized structures for each enantiomer using MOPAC on CHEM 3D. [MOPAC is a semi-empirical calculation supplied with the CambridgeSoft CS ChemOffice Pro software package (CambridgeSoft Corporation, 100 CambridgePark Drive, Cambridge, MA, 02140, USA). Energy minimization employed Austin Model 1 (AM1) theory using a restricted wave function with minimum RMS gradient set to 0.100]

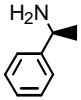
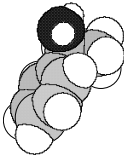
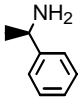
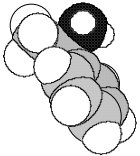
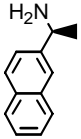
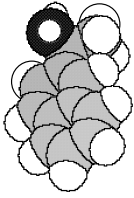
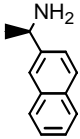
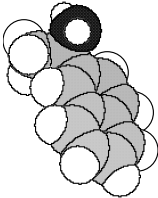
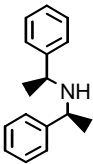
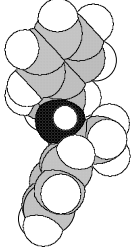
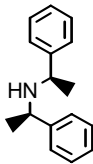
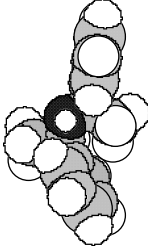
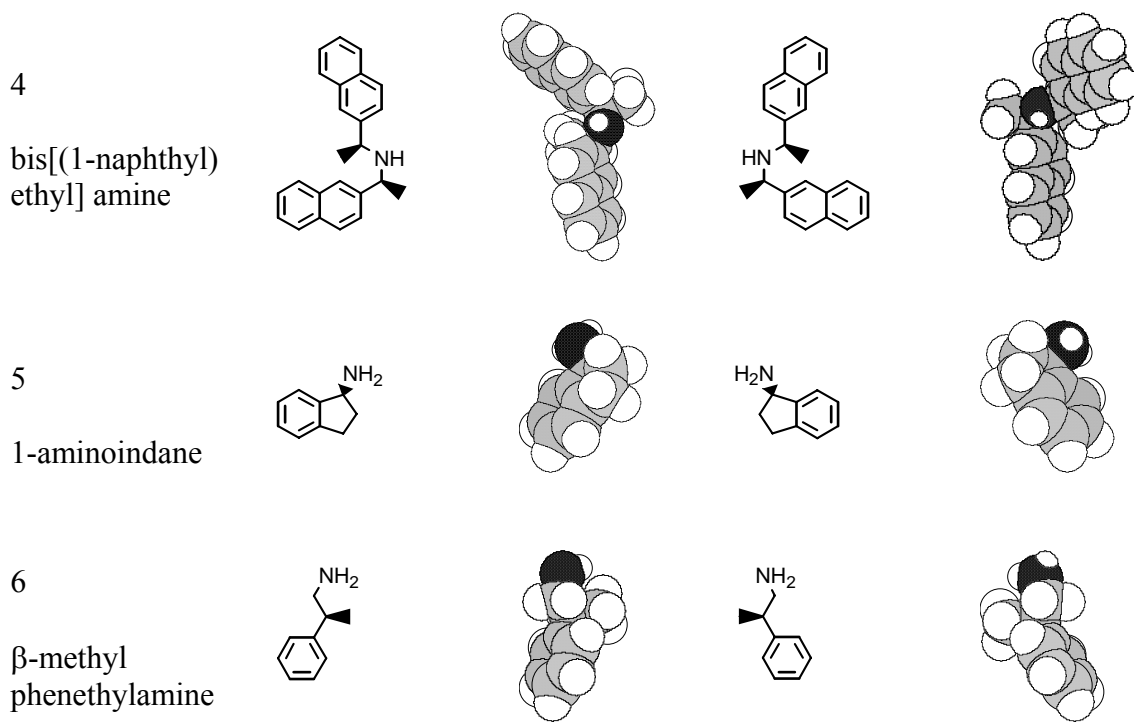
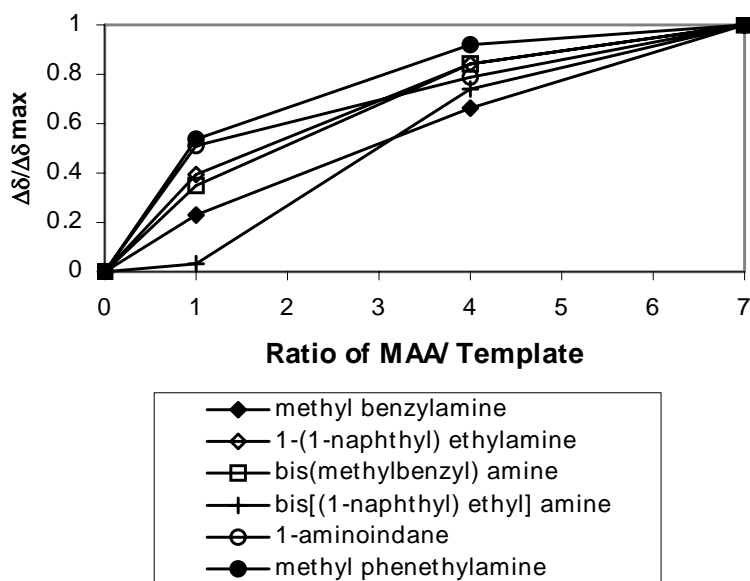
Entry	S Enantiomer	S Enantiomer	R Enantiomer	R Enantiomer
1 $\alpha$ -methyl benzyl amine				
2 1-(1-naphthyl) ethylamine				
3 bis( $\alpha$ -methyl benzyl) amine				

Table Continued



To ensure the differences in selectivity were not due to ionic interactions the  $pK_a$  values were obtained for each of the amines. All  $pK_a$  values were within a similar range (7.1-9.2). NMR verified the presence of the pre-polymer complexes. The  $^1H$  NMR titrations of the complexes in chloroform for protons located  $\alpha$  to the amine functionality are shown in figure 3. The ratio of MAA : template amine in this study was 4 : 1. The NMR shifts indicate that the amines are all interacting with the MAA to form some kind of pre-polymer complex.

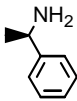
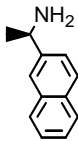
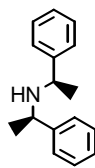
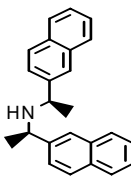
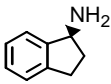
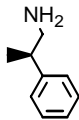
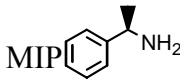
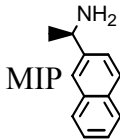
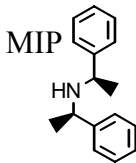
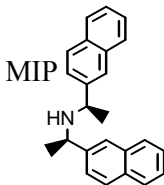
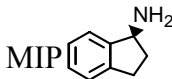
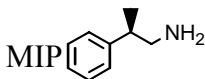
Imprinted polymers were synthesized using the S-enantiomer of each chiral amine, and the specificity of the polymers was observed by HPLC assays of both the R- and the S-enantiomers. The separation values ( $\alpha$ ) for each of the chiral amines are shown in table 2.2. With all the imprinted polymers, the highest affinity was always seen for target molecule originally used for imprinting the polymer.



**Figure 2.2.**  $^1\text{H}$  NMR titration curves for various MAA:template ratios in chloroform.

By increasing the size of the steric groups bound on the target molecule one carbon away from the chiral center from a benzyl group to a naphthyl group the selectivity is increased almost two-fold ( $\alpha = 1.33$  for benzyl versus  $\alpha = 1.58$  for naphthyl). A similar effect of increased selectivity is observed when the templates differ by two chiral centers, a molecule one carbon away from the chiral center changed in size from benzyl groups to naphthyl groups ( $\alpha = 2.26$  versus  $\alpha = 3.25$ ). In both cases some cross reactivity is seen between similar polymers. The 1-(1-naphthyl) methylamine imprinted polymer showed cross reactivity with all of the other amines with the exception of the 1-aminoindane. This implies that it may be a good structure for imprinting when a generic binding effect is needed. Increasing the number of chiral centers  $\alpha$  to the primary binding interaction from one site to two increases the selectivity approximately four-fold for both the benzyl and the naphthyl substituents ( $\alpha = 1.33$  versus  $\alpha = 2.26$  and  $\alpha = 1.58$  versus  $\alpha = 3.25$  respectively).

**Table 2.2** Separation factors ( $\alpha$ ) for the different chiral amines on each imprinted polymer.

Substrates						
MIP's						
	<b>1.33</b>	1.20	1.00	1.00	1.00	1.00
	1.23	<b>1.58</b>	1.14	1.16	1.00	1.07
	1.00	1.00	<b>2.26</b>	1.78	1.00	1.00
	1.00	1.00	1.65	<b>3.25</b>	1.00	1.00
	1.05	1.03	1.00	1.05	<b>1.44</b>	1.01
	1.00	1.01	1.00	1.00	1.02	<b>1.13</b>
Control	1.00	1.00	1.00	1.00	1.00	1.00

There is no cross reactivity between the polymers imprinted with target molecules with two chiral centers and those containing one. The bis-substituted amines are most likely sterically excluded from the binding sites of the mono-substituted amines, but the lack of selectivity of the mono-substituted amines in the polymers imprinted with the bis-substituted amines is harder to explain. It is most likely due to a difference in conformational shape of the bis- and mono-substituted amines.<sup>17</sup>

Also imprinted in this study was 1-aminoindane, which was used as a locked conformation of  $\alpha$ -methylbenzylamine. These polymers did not show the cross-reactivity with the  $\alpha$ -methylbenzylamine as expected, which suggest a different conformational state of the two molecules. The 1-aminoindane did show slightly increased separation of its own enantiomer most likely due to the locked conformational state, the increase steric hindrance, or a combination of the two effects. In order to determine the effect of distance between the primary binding event and the chiral center  $\alpha$ -methylbenzylamine can be compared with  $\beta$ -methylbenzylamine. As expected the separation factor decreases from 1.33 for the  $\alpha$ -methylbenzylamine to 1.13  $\beta$ -methylbenzylamine. It can be imagined that the closer contact of the binding amine to the stereocenter leads to a greater steric repulsion of the incorrect enantiomer.

## Chapter 3

### Optimal Spatial Fit and Shape Selectivity

### 3.1 Introduction

In order to further study the effects of sterics in MIPs a larger number of steric interactions were examined. The previous study has shown  $\alpha$ -methylbenzylamine derivatives to be good candidates for study, and they can be synthesized so only one side chain on the  $\alpha$ -methylbenzylamine derivatives changes to investigate representative changes of one hydrocarbon group at a time. The preparation of several secondary amines by the reductive amination of ketones and aldehydes using sodium triacetoxyborohydride and (S)-(-)- $\alpha$ -methylbenzylamine has been achieved in order to study systematically steric binding in molecularly imprinted polymers. This study includes a variety of secondary amines with varying alkyl chains. The steric study will examine the effect of chain size, length, and conformational restraint on the binding strength and selectivity of the target molecule, and show the concept of the optimal spatial fit (OSF) of the template. The working hypothesis of binding site structure in molecularly imprinted polymers is based on the idea that the pre-polymer complex is "locked" into place by polymerization. This assumption postulates the formation of a cavity with functional groups in a complementary array for convergent interactions with the template. With this picture in mind, selective molecular recognition for the template upon rebinding by imprinted polymers has then been attributed to both the cooperative binding of two or more pre-organized functional groups, energetically favoring the template molecule and the shape selectivity of the binding cavity that is complementary to the template. The overall significance of these two recognition elements have not been studied for molecularly imprinted polymers (MIPs). This report presents a systematic

study of structurally similar molecular probes to investigate the role of shape selectivity in MIPs and the underlying principles governing this interaction. To study the shape effect twelve similar chiral secondary amines were prepared and molecularly imprinted polymers were made. Both chiral enantiomers of these amines were cross run on the twelve MIPs and the results were analyzed.

## 3.2 Experimental

### 3.2.1 Materials

Ethylene glycol dimethacrylate (EGDMA, Polysciences) as received, was distilled in vacuo (94°C) over boiling chips prior to polymerization. Methacrylic acid was (MAA, Aldrich) was distilled over CaH<sub>2</sub> (80°C). (*R*)-(+)- $\alpha$ -methylbenzyl amine, (*S*)-(-)- $\alpha$ -methylbenzyl amine, (*R*)-(+)-*N*,  $\alpha$ -dimethylbenzylamine (**1-R**), (*S*)-(-)-*N*,  $\alpha$ -dimethylbenzylamine (**1-S**), butaldehyde, cyclohexanone, cyclopentanone, hexanal, isobutraldehyde, isovaleraldehyde, octyl aldehyde, trimethyl acetaldehyde, 1-iodopropane, 2-iodopropane, iodoethane, 1,3-dimethyl-3,4,5,6-tetrahydro-2(1H)-pyrimidinone (DMPU), and 2,2'-azobisisobutyronitrile (AIBN) were all purchased from Aldrich Chemicals and used without further purification. Sodium bicarbonate, MgSO<sub>4</sub> and all solvents were HPLC grade and obtained from Fisher Scientific. They were used without further purification.

### 3.2.2 Synthesis

The following compounds were synthesized using published methods of monoalkylation in DMPU using the proper enantiomer of  $\alpha$ -methylbenzyl amine<sup>18</sup>: (*R*)-(+)-*N*-ethyl-*N*-(1-phenylethyl)amine (**2-R**), (*S*)-(-)-*N*-ethyl-*N*-(1-phenylethyl)amine (**2-S**), (*R*)-(+)-*N*-propyl-*N*-(1-phenylethyl)amine (**3-R**), (*S*)-(-)-*N*-propyl-*N*-(1-

*phenylethylamine (3-S)*, *(R)-(+)-N-(1-phenylethyl)propan-2-amine (4-R)*, and *(S)-(-)-N-(1-phenylethyl)propan-2-amine (4-S)*. While the following compounds were synthesized by reductive amination<sup>19</sup>: *(R)-(+)-N-(1-phenylethyl)butan-1-amine (5-R)*, *(S)-(-)-N-(1-phenylethyl)butan-1-amine (5-S)*, *(R)-(+)-N-isobutyl-N-(1-phenylethyl)amine (6-R)*, *(S)-(-)-N-isobutyl-N-(1-phenylethyl)amine (6-S)*, *(R)-(+)-N-neopentyl-N-(1-phenylethyl)amine (7-R)*, *(S)-(-)-N-neopentyl-N-(1-phenylethyl)amine (7-S)*, *(R)-(+)-N-(3-methylbutyl)-N-(1-phenylethyl)amine (8-R)*, *(S)-(-)-N-(3-methylbutyl)-N-(1-phenylethyl)amine (8-S)*, *(R)-(+)-N-(1-phenylethyl)cyclopentanamine (9-R)*, *(S)-(-)-N-(1-phenylethyl)cyclopentanamine (9-S)*, *(R)-(+)-N-(1-phenylethyl)hexan-1-amine (10-R)*, *(S)-(-)-N-(1-phenylethyl)hexan-1-amine (10-S)*, *(R)-(+)-N-(1-phenylethyl)cyclohexanamine (11-R)*, *(S)-(-)-N-(1-phenylethyl)cyclohexanamine (11-S)*, *(R)-(+)-N-(1-phenylethyl)octan-1-amine (12-R)*, and *(S)-(-)-N-(1-phenylethyl)octan-1-amine (12-S)*. All synthesized compounds were purified over silica gel using a 15/5/1: hexane/ethyl acetate/triethylamine mixture. *N*-ethyl-*N*-(1-phenylethyl)amine (**2**),<sup>20</sup> *N*-(1-phenylethyl)propan-2-amine (**4**) and *N*-neopentyl-*N*-(1-phenylethyl)amine (**7**),<sup>18</sup> *N*-(1-phenylethyl)butan-1-amine (**5**),<sup>21</sup> *N*-(1-phenylethyl)cyclopentanamine (**9**),<sup>22</sup> and *N*-(1-phenylethyl)cyclohexanamine (**11**)<sup>23</sup> have been previously characterized.

#### Spectral Data:

**2-R** *(R)-(+)-N-ethyl-N-(1-phenylethyl)amine*

<sup>1</sup>HNMR(CDCl<sub>3</sub>): δ (ppm) 1.09(t, 3H, CH<sub>3</sub>) 1.39(d, 3H, CH<sub>3</sub>) 2.63(m, 2H, CH<sub>2</sub>) 3.92(q, 1H, CH-Ar) 7.32(m, 5H, Ar)

**2-S** *(S)-(-)-N-ethyl-N-(1-phenylethyl)amine*

<sup>1</sup>HNMR(CDCl<sub>3</sub>): δ (ppm) 1.09(t, 3H, CH<sub>3</sub>) 1.39(d, 3H, CH<sub>3</sub>) 2.63(m, 2H, CH<sub>2</sub>) 3.92(q, 1H, CH-Ar) 7.32(m, 5H, Ar)

**3-R** *(R)-(+)-N-propyl-N-(1-phenylethyl)amine*

IR (cm<sup>-1</sup>) 700, 761, 1132, 1368, 1451, 1492, 2802, 2873, 2929, 2959, 3025

<sup>1</sup>HNMR(CDCl<sub>3</sub>): δ (ppm) 0.90(t, 3H, CH<sub>3</sub>) 1.38(d, 3H, CH<sub>3</sub>) 1.50(m, 2H, CH<sub>2</sub>) 2.47(m, 2H, CH<sub>2</sub>) 3.79(q, 1H, CH-Ar) 7.33(m, 5H, Ar) <sup>13</sup>CNMR: δ (ppm) 12.2, 23.8, 24.8, 50.2, 58.8, 127.0, 127.2, 128.8, 146.3.

Calculated m/z: 163.263 Found LRMS(m<sup>+</sup>): 163.

**3-S** *(S)-(-)-N-propyl-N-(1-phenylethyl)amine*

<sup>1</sup>HNMR(CDCl<sub>3</sub>): δ (ppm) 0.90(t, 3H, CH<sub>3</sub>) 1.38(d, 3H, CH<sub>3</sub>) 1.50(m, 2H, CH<sub>2</sub>) 2.47(m, 2H, CH<sub>2</sub>) 3.79(q, 1H, CH-Ar) 7.33(m, 5H, Ar)

**4-R** *(R)-(+)-N-(1-phenylethyl)propan-2-amine*

<sup>1</sup>HNMR(CDCl<sub>3</sub>): δ (ppm) 1.02(t, 6H, CH<sub>3</sub>) 1.36(d, 3H, CH<sub>3</sub>) 2.66(m, 1H, CH) 3.94(q, 1H, CH-Ar) 7.33(m, 5H, Ar)

**4-S** *(S)-(-)-N-(1-phenylethyl)propan-2-amine*

<sup>1</sup>HNMR(CDCl<sub>3</sub>): δ (ppm) 1.02(t, 6H, CH<sub>3</sub>) 1.36(d, 3H, CH<sub>3</sub>) 2.66(m, 1H, CH) 3.94(q, 1H, CH-Ar) 7.33(m, 5H, Ar)

**5-R** *(R)-(+)-N-(1-phenylethyl)butan-1-amine*

<sup>1</sup>HNMR(CDCl<sub>3</sub>): δ (ppm) 0.90(t, 3H, CH<sub>3</sub>) 1.39(d, 3H, CH<sub>3</sub>) 1.50 (m, 4H, CH<sub>2</sub>CH<sub>2</sub>) 2.45(m, 2H, CH<sub>2</sub>) 3.75(q, 1H, CH-Ar) 7.34(m, 5H, Ar)

**5-S** *(S)-(-)-N-(1-phenylethyl)butan-1-amine*

<sup>1</sup>HNMR(CDCl<sub>3</sub>): δ (ppm) 0.90(t, 3H, CH<sub>3</sub>) 1.39(d, 3H, CH<sub>3</sub>) 1.50 (m, 4H, CH<sub>2</sub>CH<sub>2</sub>) 2.45(m, 2H, CH<sub>2</sub>) 3.75(q, 1H, CH-Ar) 7.34(m, 5H, Ar)

**6-R** *(R)-(+)-N-isobutyl-N-(1-phenylethyl)amine*

IR (cm<sup>-1</sup>) 700, 760, 1128, 1171, 1368, 1471, 1492, 2808, 2870, 2957, 3025

<sup>1</sup>HNMR(CDCl<sub>3</sub>): δ (ppm) 0.90(d, 6H, CH<sub>3</sub>) 1.40(d, 3H, CH<sub>3</sub>) 1.76(m, 1H, CH(CH<sub>3</sub>)<sub>2</sub>)

2.25(m, 2H, CH<sub>2</sub>) 3.81(q, 1H, CH-Ar) 7.35(m, 5H, Ar) <sup>13</sup>CNMR: δ (ppm) 21.0, 21.2,

24.8, 26.5, 56.2, 58.8, 127.0, 127.2, 128.8, 146.3. Calculated m/z: 178.297 Found

LRMS(m<sup>+</sup>): 177.

**6-S** *(S)-(-)-N-isobutyl-N-(1-phenylethyl)amine*

<sup>1</sup>HNMR(CDCl<sub>3</sub>): δ (ppm) ) 0.90(d, 6H, CH<sub>3</sub>) 1.40(d, 3H, CH<sub>3</sub>) 1.76(m, 1H, CH(CH<sub>3</sub>)<sub>2</sub>)

2.25(m, 2H, CH<sub>2</sub>) 3.81(q, 1H, CH-Ar) 7.35(m, 5H, Ar)

**7-R** *(R)-(+)-N-neopentyl-N-(1-phenylethyl)amine*

<sup>1</sup>HNMR(CDCl<sub>3</sub>): δ (ppm) 1.08(s, 9H, CH<sub>3</sub>) 1.50(d, 3H, CH<sub>3</sub>) 2.36(dd, 2H,CH<sub>2</sub>) 3.87(q,

1H, CH-Ar) 7.47(m, 5H, Ar)

**7-S** *(S)-(-)-N-neopentyl-N-(1-phenylethyl)amine*

<sup>1</sup>HNMR(CDCl<sub>3</sub>): δ (ppm) 1.08(s, 9H, CH<sub>3</sub>) 1.50(d, 3H, CH<sub>3</sub>) 2.36(dd, 2H,CH<sub>2</sub>) 3.87(q,

1H, CH-Ar) 7.47(m, 5H, Ar)

**8-R** *(R)-(+)-N-(3-methylbutyl)-N-(1-phenylethyl)amine*

IR (cm<sup>-1</sup>) 555, 594, 700, 760, 1028, 1076, 1129, 1207, 1366, 1451, 1492, 1603, 2868,

2924, 2956, 3025, 3062 <sup>1</sup>HNMR(CDCl<sub>3</sub>): δ (ppm) 0.87(t, 3H, CH<sub>3</sub>) 1.39(d, 3H, CH<sub>3</sub>)

1.42 (m, 2H, CH<sub>2</sub>) 1.61(m, 1H,CH<sub>2</sub>(CH<sub>3</sub>)<sub>2</sub>) 2.47(m, 2H, CH<sub>2</sub>) 3.75(q, 1H, CH-Ar)

7.32(m, 5H, Ar) <sup>13</sup>CNMR: δ (ppm) 22.8, 23.0, 24.8, 26.6, 39.9, 59.3, 126.8, 127.3, 128.9,

146.3. Calculated m/z: 191.316 Found LRMS(m<sup>+</sup>): 191.

**8-S** *(S)-(-)-N-(3-methylbutyl)-N-(1-phenylethyl)amine*

<sup>1</sup>HNMR(CDCl<sub>3</sub>): δ (ppm) 0.87(t, 3H, CH<sub>3</sub>) 1.39(d, 3H, CH<sub>3</sub>) 1.42 (m, 2H, CH<sub>2</sub>) 1.61(m, 1H,CH<sub>2</sub>(CH<sub>3</sub>)<sub>2</sub>) 2.47(m, 2H, CH<sub>2</sub>) 3.75(q, 1H, CH-Ar) 7.32(m, 5H, Ar)

**9-R** *(R)-(+)-N-(1-phenylethyl)cyclopentanamine*

<sup>1</sup>HNMR(CDCl<sub>3</sub>): δ (ppm) 1.20-1.60(m, 4H, CH<sub>2</sub>CH<sub>2</sub>) 1.37(d, 3H, CH<sub>3</sub>) 1.60-1.90 (m, 4H, CH<sub>2</sub>CH<sub>2</sub>) 2.90(m, 1H, CH) 3.88(q, 1H, CH-Ar) 7.32(m, 5H, Ar)

**9-S** *(S)-(-)-N-(1-phenylethyl)cyclopentanamine*

<sup>1</sup>HNMR(CDCl<sub>3</sub>): δ (ppm) 1.20-1.60(m, 4H, CH<sub>2</sub>CH<sub>2</sub>) 1.37(d, 3H, CH<sub>3</sub>) 1.60-1.90 (m, 4H, CH<sub>2</sub>CH<sub>2</sub>) 2.90(m, 1H, CH) 3.88(q, 1H, CH-Ar) 7.32(m, 5H, Ar)

**10-R** *(R)-(+)-N-(1-phenylethyl)hexan-1-amine*

IR (cm<sup>-1</sup>) 555, 595, 700, 761, 1077, 1130, 1305, 1368, 1451, 1492, 1603, 2357, 2856, 2926, 2957, 3025, 3083, 3083 <sup>1</sup>HNMR(CDCl<sub>3</sub>): δ (ppm) 0.90(t, 3H, CH<sub>3</sub>) 1.28(m, 6H, CH<sub>2</sub>CH<sub>2</sub>CH<sub>2</sub>) 1.35(d, 3H, CH<sub>3</sub>) 1.50(m, 2H, CH<sub>2</sub>) 2.50(m, 2H, CH<sub>2</sub>) 3.76(q, 1H, CH-Ar) 7.33(m, 5H, Ar) <sup>13</sup>CNMR: δ (ppm) 14.4, 23.0, 24.8, 27.5, 30.7, 32.3, 48.4, 59.4, 126.8, 127.3, 128.1, 146.3. Calculated m/z:205.343 Found HRMS:205.1822

**10-S** *(S)-(-)-N-(1-phenylethyl)hexan-1-amine*

<sup>1</sup>HNMR(CDCl<sub>3</sub>): δ (ppm) 0.90(t, 3H, CH<sub>3</sub>) 1.28(m, 6H, CH<sub>2</sub>CH<sub>2</sub>CH<sub>2</sub>) 1.35(d, 3H, CH<sub>3</sub>) 1.50(m, 2H, CH<sub>2</sub>) 2.50(m, 2H, CH<sub>2</sub>) 3.76(q, 1H, CH-Ar) 7.33(m, 5H, Ar)

**11-R** *(R)-(+)-N-(1-phenylethyl)cyclohexanamine*

<sup>1</sup>HNMR(CDCl<sub>3</sub>): δ (ppm) 1.05(m, 6H, CH<sub>2</sub>CH<sub>2</sub>CH<sub>2</sub>) 1.33(d, 3H, CH<sub>3</sub>) 1.56-2.0 (m, 4H, CH<sub>2</sub>CH<sub>2</sub>) 2.30(m, 1H, CH) 3.98(q, 1H, CH-Ar) 7.31(m, 5H, Ar)

**11-S** *(S)-(-)-N-(1-phenylethyl)cyclohexanamine*

$^1\text{H NMR}(\text{CDCl}_3)$ :  $\delta$  (ppm) 1.05(m, 6H,  $\text{CH}_2\text{CH}_2\text{CH}_2$ ) 1.33(d, 3H,  $\text{CH}_3$ ) 1.56-2.0 (m, 4H,  $\text{CH}_2\text{CH}_2$ ) 2.30(m, 1H, CH) 3.98(q, 1H, CH-Ar) 7.31(m, 5H, Ar)

**12-R** (*R*)-(+)-*N*-(1-phenylethyl)octan-1-amine

IR ( $\text{cm}^{-1}$ ) 556, 593, 700, 760, 1027, 1077, 1131, 1304, 1351, 1368, 1451, 1466, 1492, 2854, 2924, 2957, 3025, 3062, 3310  $^1\text{H NMR}(\text{CDCl}_3)$ :  $\delta$  (ppm) 0.90(t, 3H,  $\text{CH}_3$ ) 1.28(m, 8H,  $\text{CH}_2\text{CH}_2\text{CH}_2\text{CH}_2$ ) 1.35(d, 3H,  $\text{CH}_3$ ) 1.50(m, 2H,  $\text{CH}_2$ ) 2.50(m, 2H,  $\text{CH}_2$ ) 3.76(q, 1H, CH-Ar) 7.33(m, 5H, Ar)  $^{13}\text{C NMR}$ :  $\delta$  (ppm) 14.5, 23.1, 24.8, 27.8, 29.7, 30.0, 32.2, 32.5, 48.3, 58.9, 126.8, 127.0, 128.1, 146.3. Calculated  $m/z$ : 233.2143. Found HRMS: 233.2153.

**12-S** (*S*)-(-)-*N*-(1-phenylethyl)octan-1-amine

$^1\text{H NMR}(\text{CDCl}_3)$ :  $\delta$  (ppm) 0.90(t, 3H,  $\text{CH}_3$ ) 1.28(m, 8H,  $\text{CH}_2\text{CH}_2\text{CH}_2\text{CH}_2$ ) 1.35(d, 3H,  $\text{CH}_3$ ) 1.50(m, 2H,  $\text{CH}_2$ ) 2.50(m, 2H,  $\text{CH}_2$ ) 3.76(q, 1H, CH-Ar) 7.33(m, 5H, Ar)

### 3.2.3 Polymer Preparation

The following procedure was used for all imprinted polymers. In a borosilicate scintillation vial, 1.28 mmol of the S enantiomer of the chiral amine was dissolved in 8.0 mL methylene chloride. To this solution was added 5.0 g EGDMA (25.2 mmol), 0.53 g MAA (6.3 mmol) and 0.11 g (0.64 mmol) AIBN. The control polymer was formulated in a similar fashion, without introduction of a template molecule. Each solution was separated into three 13mm x 100mm screw cap tubes and each tube purged by bubbling nitrogen gas into the mixture for 5 minutes, then capped and sealed with teflon tape and parafilm. The samples were inserted into a photochemical turntable reactor (ACE Glass Inc.) which was immersed in a constant temperature bath. A standard laboratory UV light source (a Canrad-Hanovia medium pressure 450 W mercury arc lamp) jacketed in a

borosilicate double-walled immersion well was placed at the center of the turntable. The polymerization was initiated photochemically at 20°C and the temperature maintained by both the cooling jacket surrounding the lamp and the constant temperature bath holding the entire apparatus. The polymerization was allowed to proceed for 10 h, then used for chromatographic experiments. It should be noted here that the ratio of MAA to print molecule was 4:1 which has been found to be optimum in other investigations of imprinted polymers.<sup>24</sup>

### 3.2.4 Chromatographic Experiments

The polymers were ground using a mortar and pestle, the particles were sized using U.S.A. Standard Testing Sieves (VWR), and the fraction between 20-25  $\mu\text{m}$  was collected. The particles were slurry packed, using a Beckman 1108 Solvent Delivery Module, into stainless steel columns (length, 10.0 cm, i.d. 4.6 mm) to full volume (approximately 0.6 g of polymer) for chromatographic experiments. The polymers were then equilibrated online. HPLC analyses were performed isocratically at room temperature (22°C) using a Hitachi L-7100 pump with a Hitachi L-7400 detector. The flow rate in all cases was set at 1.0 mL/min using a mobile phase consisting of acetonitrile/water/acetic acid: 93/5/2 with a Uv detector at a wavelength of 262 nm. Sample injections were 5  $\mu\text{L}$ , of a 1.0 mM solution of amine in acetonitrile. Each sample was injected at least twice on each column with a wash of 90/10 acetonitrile/acetic acid run between each injection to remove any residual analyte. Retention times were recorded with an error of 0.05 minutes. The void volume was determined using acetone as an inert substrate. The separation factors ( $\alpha$ ) were measured as the ratio of capacity

factors ( $k'_S/k'_R$ ). The capacity factors were determined by the relation  $k' = (R_v - D_v) / D_v$ , where  $R_v$  is the retention volume of the substrate, and  $D_v$  is the void volume.

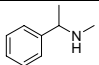
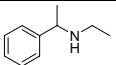
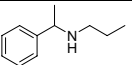
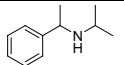
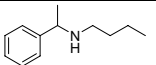
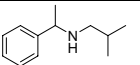
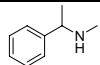
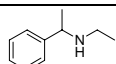
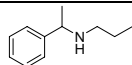
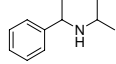
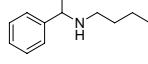
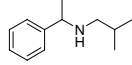
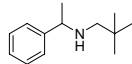
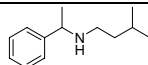
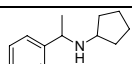
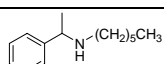
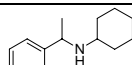
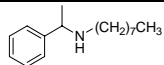
### 3.3 Results and Discussion

The MIPs separation factor,  $\alpha$ , for each molecular probe on each of the imprinted polymers was obtained by HPLC.<sup>25</sup> The table of  $\alpha$  values is shown in table 3.1, which shows a number of informative trends. As expected the maximum  $\alpha$  value for most of the imprinted polymers is found for the molecule the polymer was templated<sup>25</sup> (which will be referred to as the "template  $\alpha$ " values and are shown in bold in a diagonal fashion in table) with the exception of compound 12 which will be discussed later. A second trend is that all analytes larger than a specified template have reduced selectivity by the MIP of that template. This indicates a steric exclusion effect for analytes larger than the template analyte. Steric interactions in the binding site can also explain the overall separation of chiral amines with only one functional interaction.

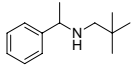
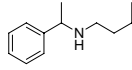
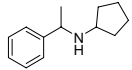
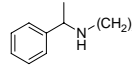
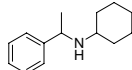
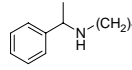
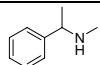
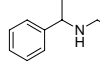
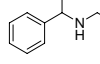
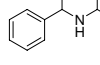
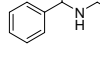
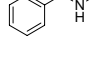
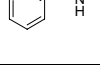
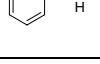
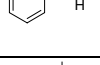
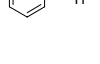
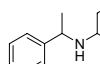
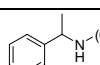
As the number of carbons in the side chain of the molecular probes increases past the number in the original template molecule, there is a corresponding decrease in the selectivity. Therefore, the imprinted binding site appears to form a binding cavity; and that cavity physically restricts access to molecular components larger than the space of the cavity. It is difficult to quantify binding energy differences for the imprinted site for each molecular probe due to heterogeneity of binding sites, but the relative trends do appear consistent.

The selectivity is more complex to describe in cases where the molecular probe is roughly the same size or smaller than the template molecule. This implies that shape

**Table 3.1a.** Separation factors ( $\alpha$ ) for the enantioselectivity of each molecular probe on each imprinted polymer.

Analyte --> Polymer						
	<b>1.38</b>	1.37	1.26	1.13	1.09	1.17
	1.22	<b>1.51</b>	1.32	1.25	1.29	1.28
	1.18	1.38	<b>1.43</b>	1.39	1.42	1.38
	1.04	1.86	1.43	<b>2.41</b>	1.77	1.64
	1.17	1.5	1.45	1.18	<b>1.66</b>	1.60
	1.04	1.32	1.58	1.44	1.48	<b>1.65</b>
	1.03	1.27	1.24	1.28	1.24	1.39
	1.19	1.35	1.28	1.29	1.41	1.37
	1.10	1.58	1.50	1.84	1.39	1.45
	1.09	1.45	1.29	1.36	1.43	1.39
	1.14	1.35	1.39	1.76	1.53	1.54
	1.06	1.39	1.26	1.31	1.38	1.38
Control	1.0	1.0	1.0	1.0	1.0	1.0

**Table 3.1b.** Separation factors ( $\alpha$ ) for the enantioselectivity of each molecular probe on each imprinted polymer.

Analyte --> Polymer						
	1.02	1.11	1.02	1.09	1.01	1.00
	1.17	1.24	1.29	1.34	1.16	1.17
	1.19	1.31	1.31	1.35	1.26	1.23
	1.15	1.38	1.83	1.40	1.63	1.27
	1.08	1.50	1.57	1.37	1.58	1.21
	1.33	1.42	1.56	1.24	1.55	1.21
	<b>1.52</b>	1.26	1.27	1.29	1.28	1.11
	1.23	<b>1.42</b>	1.27	1.35	1.31	1.20
	1.1	1.54	<b>1.94</b>	1.39	1.83	1.37
	1.31	1.32	1.22	<b>1.49</b>	1.24	1.26
	1.32	1.85	1.85	1.44	<b>2.53</b>	1.29
	1.08	1.37	1.33	1.47	1.20	<b>1.20</b>
Control	1.0	1.0	1.0	1.0	1.0	1.0

selectivity is due to interaction of the molecular probe with the interior of the binding cavity, i.e. with the matrix walls of the binding cavity. Minimal interactions of the molecular probe with the interior of the binding cavity is not anticipated to afford much selectivity, instead molecules or substructures of molecules can move around freely within the cavity with no molecular recognition taking place. Conversely, maximizing interactions of the molecular probe with the interior of the binding cavity should maximize latent selectivity, which is effectively matching a template with a cavity of complementary shape. The side chain groups in this study have different amounts of branching creating a bulkier shape, that is somewhat rounded at the surface due to conformational rotation of all the bonds. If the structures are cyclic, conformational space is limited, presenting a flatter and more topologically defined combination of atoms, especially if the ring is aromatic. The better the contact between template shape and cavity shape, the more contacts there are for defining selectivity better. These concepts for shape selectivity in MIPs can be summarized as follows:

- Van der Waals interactions are responsible for increased selective binding due to increasing binding energy of best fit analytes.
- The more accommodating the shape complementarity, the greater will the number of contacts between molecular probe and MIP binding site, which will increase selectivity. This is defined as "optimal spatial fit."
- Molecular probes smaller than the binding site cavity, or molecules with greater conformational flexibility in the binding site, will decrease selectivity. This is referred to as a "non-optimal spatial fit."

The best fit of a substrate into the binding cavity of an MIP would afford the maximum number of contact interactions, and is referred to as the "optimal spatial fit" (OSF). A substrate that cannot obtain the maximum number of interactions has a "non-optimal spatial fit" (non-OSF), which results in a lowering of binding affinity and to a greater extent selectivity.

The most accurate diagnostic of optimal or non-optimal spatial fit is the loss of three dimensional recognition, using  $\alpha$  values as the figure of merit. The separation factors in table 3.1 show that the highest  $\alpha$  values found for each MIP corresponds to the template molecule, which are shown in bold. This supports the theory that MIP binding cavities are shape selective, since the template would be anticipated to have the maximum number of complementary contact interactions for a binding site imprinted around that template. The molecular probes in tables 3.1 are organized in order of increasing size of template molecule making it easy to identify size-related trends. The highest  $\alpha$  values correspond to the OSF and are shown in bold and form a diagonal from the top left to the bottom right in each table. This diagonal is the dividing point for the different interactions of the molecular probes. The values above the diagonal indicate less than optimal selectivity attributed to steric exclusion effects of probes larger than the template molecule. The values below the diagonal indicate decreasing selectivity due to non-optimal spatial fit, with the lowest values corresponding to small molecular probe side chains interacting with MIPs made with templates having large side chains.

The influence of the side chain size appears to be dependent on the distance from the amine binding group which the primary binding interaction of the template with the polymer. For example the side chains in compounds 4, 9, and 11 have a secondary

carbon, or branch point, directly attached to the amine. This creates an environment of greater surface area for Van der Waals interactions near the primary binding interaction, which has resulted in considerably higher "template  $\alpha$ " values for these three compounds. The further away the branch points are from the primary binding interaction, the less pronounced the effect will be on the "template  $\alpha$ " value, as seen for compounds 6, 7, and 8. Although the data are limited, comparison of compounds 6, 7, and 8 appears to indicate slightly better selectivity for secondary carbon branches (6,8) versus tertiary carbon branches (7); which may be an entropic effect due to the secondary branched carbons having fewer degenerate conformational states.

Another general trend is that straight-chain groups give the lowest "template  $\alpha$ " values; for example, compounds 1, 2, 3, 5, 10, and 12 all have considerable lower separation factors versus the branched compounds. Entropic factors are most likely the reason for this, with the conformational flexibility of the straight-chain groups lowering the overall rebinding energy of the molecular probe with a corresponding decrease in selectivity (a "non-optimal spatial fit"). The straight-chain octyl group in compound 12 presents a special case. This compound is relatively ineffective at imprinting polymers with any significant recognition as shown by the low separation factors for all compounds on this MIP; in addition, it shows relatively low binding on all polymers. This may be due to the large number of conformational states available to the n-octyl chain of compound 12, thus limiting selectivity in hydrocarbon chains that have less than eight carbons. Another example of decreasing molecular recognition due to conformational entropy is seen comparing the lower template  $\alpha$  value of compound 10 with the n-hexyl side chain versus compound 5 incorporating a n-butyl side chain.

An important observation from this study is the determinant role Van der Waals interactions play in the *selective* binding of molecules to MIP binding sites. These interactions are not considered influential in the solution phase pre-polymer complex due to weak interactions. Instead, Van der Waals interactions only appear to come into play *after* the polymer is made. Therefore, direct correlation of solution phase pre-polymer complex may not accurately predict selectivity in MIPs. The working hypothesis in scheme 1 may still be an accurate illustration of the polymer imprinting strategy, since shape selectivity is depicted. However, these findings suggest that the crosslinking monomers are an active part of imprinting, rather than merely an "inert" scaffolding for functional monomers.

#### 3.4. Summary and Conclusion

Quantitative structure-binding relationships between  $\alpha$ -methylbenzylamine derivatives have provided evidence for shape selectivity in non-covalently imprinted polymers. Shape selectivity is determined by steric exclusion or an "optimal spatial fit" which maximizes binding interactions. Unique branching architectures provide better selectivity versus straight chain hydrocarbons, with complete loss of recognition by straight chain groups with eight or more carbons. Last, the importance of shape selectivity to molecular recognition by MIPs highlights the importance of the supporting matrix and complicates predictions of selective binding from the solution structure of pre-polymer complexes.

## Chapter 4

# Structural Changes and Aggregation of Human Influenza Virus

## 4.1 Introduction

The human influenza virus has been a common cause of illness and death for several centuries. The influenza pandemic that occurred in the early part of the twentieth century is estimated to have resulted in between 20 and 50 million deaths.<sup>26</sup> The two strains of influenza virus selected for this study, X-31 and PR-8, have been widely used in laboratory research. Much is known about their genome and protein composition. Each virus particle consists of a lipid envelope, acquired from the host cell, which contains membrane proteins. The protein composition of the viral envelope of the X-31 strain of influenza has a molar ratio of the hemagglutinin fusion protein (HA) to the matrix protein (M1) to the nucleocapsid protein (NP) of 0.9:1:1.3.<sup>27</sup> The NP component is mixed with neuraminidase (NA) that has a similar molecular weight in SDS gel electrophoresis and generally is not well resolved.<sup>28</sup> The ratio of envelope proteins is similar for various strains of the virus.<sup>29,30</sup>

In the electron microscope influenza virus particles vary in size and shape, perhaps dependent on the specifics of the budding step at the end of the replication process. They typically appear to be spherical or ovoid in shape with characteristic dimensions of 800 Å to about 2000 Å. Particles are often clustered together, although it is not clear whether this is an artifact of preparation or the natural state of the parent virus suspensions. The major envelope glycoproteins, HA and NA, form “spikes” protruding from the membrane. The core of the virus contains the nucleocapsid composed of RNA and matrix proteins.

An influenza particle enters the cell by the binding of the HA spike to mucoglycoproteins and glycolipids containing sialic acid groups. This binding is reversed by the action of the viral NA that hydrolyzes the receptor. This reversibility likely facilitates the penetration of the virus further into the respiratory tract. After the virus is firmly bound, it becomes engulfed by the host cell. The resulting endosome is then acidified to approximately pH 5 through the action of an endosomal proton-ATPase. The reduction of pH causes a conformational change in the HA spike which activates membrane-fusion. The fusion of the endosome membrane with the virus envelope creates a pore that allows the genomic information to be released into the cell for uptake by the nucleus and subsequent replication.

The exact nature of the conformational change in the HA protein spike is subject to debate.<sup>31-33</sup> HA is comprised of two polypeptide chains, HA1 and HA2 that are linked by a disulfide bond. The HA1 subunit is located in the ectodomain of the virus and is responsible for binding to the sialic acid receptors on target cells. The HA2 subunit spans the viral envelope with a single transmembrane helix and contains the apparatus required for membrane fusion. Activation of HA at low pH causes a molecular rearrangement. Although this conformational change is essential for fusion of the intact virus, it is often the isolated proteins that are studied. The most detailed knowledge of the conformational change that is triggered by low pH is known from X-ray crystallographic studies of Wiley and coworkers.<sup>34-36</sup> However, in order to crystallize the protein it has been necessary to truncate the molecule. In addition, the conformational properties of a truncated form of HA in the crystalline state may not be identical to its properties when present at high concentration inserted into the viral membrane of the viral envelope. In addition, the

crystal structure of the isolated protein fragment provides no information about how the protein is oriented in the viral membrane. The morphological change upon acidification of bromelin-cleaved HA was found by electron microscopy studies to be  $\sim 50 \text{ \AA}$ .<sup>37-40</sup> There have also been other studies on the structure of the intact virus at neutral pH by electron microscopy<sup>27,41</sup> and there is evidence that the cytoplasmic tail of HA has an influence on the shape of the particle.<sup>30</sup> A neutron diffraction study on the intact virus made use of the different scattering length densities of the nucleocapsid and the viral envelope.<sup>42</sup> Electron microscopy studies on the intact virus detected much smaller changes in the length of the spikes protruding from the virus<sup>43,44</sup> compared with the studies of the ectodomain of HA<sup>37</sup>. Electron microscopy studies require freezing of the sample and the changes cannot be monitored continuously. In addition, the authors acknowledge that cryoelectron microscopy does not provide sufficient contrast to detect an extended coiled-coil region.<sup>44</sup> There appears to be no information on the rate of conformational change in the intact virus.

In this study, pH-induced changes to the intact human influenza virus are monitored by static and dynamic light scattering (SLS and DLS, respectively). In addition to comparative measurements before and well after acidification, DLS experiments at a single scattering angle are also performed in a time-resolved fashion with a resolution of about 15 s. Although this is slower than time-resolved CD measurements on the isolated HA protein,<sup>32</sup> it is of interest to know the magnitude and kinetics of changes to the HA protein when tethered to the intact virus particle. Our studies also reveal structural changes on a longer distance scale, including interactions among influenza particles.

## 4.2 Light Scattering

In DLS, the measured intensity autocorrelation function,  $g^{(2)}(t)$  obtained under homodyne, Gaussian signal conditions<sup>45,46</sup> can be related to the normalized electric field autocorrelation function,  $g^{(1)}(t)$

$$g^{(2)}(t) = 1 + f[g^{(1)}(t)]^2 \quad (1)$$

where the parameter  $f$  is, for the case of strongly scattering particles, established by optical and electrical details of the instrument ( $0 < f < 1$ ). Here,  $t$  is the lag time between observations used to compute the autocorrelation function. For monodisperse, spherical samples,  $g^{(1)}(t)$  is given by a single exponential decay,

$$g^{(1)}(t) = e^{-q^2Dt} \quad (2)$$

where  $D$  is the diffusion coefficient and  $q$  is the scattering vector magnitude ( $q = 4\pi n \sin(\theta/2) / \lambda_0$  with  $n$  = refractive index,  $\theta$  = scattering angle,  $\lambda_0$  = incident wavelength *in vacuo*). When multiple scatterers are present, the electric field autocorrelation function is a weighted sum of exponential terms, the sum running over all scattering components:

$$g^{(1)}(t) = \sum_i A_i e^{-\Gamma_i t} \quad (3)$$

In this expression, the amplitude,  $A_i$ , is proportional to concentration,  $c_i$ , and mass,  $M_i$ , of the  $i^{\text{th}}$  particle. The decay rate,  $\Gamma_i$ , is  $q^2 D_i$ , where the diffusion coefficient,  $D_i$ , is inversely related to the hydrodynamic radius,  $R_{h,i}$ , via the Stokes-Einstein relation:

$$D_i = \frac{kT}{6\pi\eta R_{h,i}} \quad (4)$$

In Eq. 4,  $k$  is Boltzmann's constant,  $T$  is the absolute temperature, and  $\eta$  is the solution viscosity. Depending on the number and relative amplitude of multiple exponential terms, the autocorrelation function may be analyzed as a single exponential, sum of

exponentials or through the cumulants approach developed by Koppel.<sup>47</sup> In this latter approach, the logarithm of  $g^{(1)}(t)$  is expressed as a polynomial:

$$\ln g^{(1)}(t) = -\bar{\Gamma}t + \frac{\mu_2}{2}t^2 + \dots \quad (5)$$

The quotient between the 2<sup>nd</sup> cumulant,  $\mu_2$ , and the square of the average decay rate,  $\bar{\Gamma}$ , indicates the heterogeneity of the sample and absence of terms not related to translational diffusion;  $\mu_2 / \bar{\Gamma}^2$  would be zero for a single diffuser of simple shape when measured at low  $q$ , such that rotational contributions or internal motions cannot be observed. Laplace inversion methods such as the program CONTIN<sup>48,49</sup> to extract the set of  $A_i$  and  $\Gamma_i$  are warranted when  $\mu_2 / \bar{\Gamma}^2$  exceeds about 0.3, given data of typical quality. Discrete, multiple exponential fitting may be successful for even smaller values of  $\mu_2 / \bar{\Gamma}^2$ .

In SLS, there are two general strategies to obtain and analyze the dependence of scattered intensity,  $I$ , as a function of  $q$ . The first is to obtain data at sufficiently low scattering angles that the radius of gyration,  $R_g$ , can be obtained using, for example, the Guinier relation:

$$\ln I = \ln I_0 - \frac{q^2 R_g^2}{3} + \dots \quad (6)$$

For most shapes, this method will produce a valid  $R_g$  if  $q_{\max} R_g$  does not much exceed unity, where  $q_{\max}$  corresponds to the highest scattering angle used (or shortest wavelength at fixed angle). An advantage of the Guinier method is that the intensity extrapolated to zero angle,  $I_0$ , does not have to be determined to obtain a size. It is merely a constant on the right side of Eq. 6. If the shape is known *a priori*, or if it is desirable to compare the scattering profile with simple models, then it may make more sense to acquire the

intensity data at higher angles and fit the particle form factor for that shape,  $P(q)$ . The particle form factor ( $0 < P(qR_g) < 1$ ) describes the reduction of intensity due to finite size of the particle:

$$I(q) = I_0 P(q) \quad (7)$$

The zero-angle intensity,  $I_0$ , is proportional to the concentration and mass of the scatterers. Typically, a nonlinear fit routine is used to adjust  $I_0$  and  $R_g$  until the theoretical  $P(q)$  expression for the assumed shape matches data collected at discrete values of  $q$ .

## 4.3 Experimental

### 4.3.1 Preparation of Virus Suspensions

Two strains of influenza virus (X-31 and PR-8) were obtained from Charles River Laboratories at a concentration of 2 mg of protein per mL of HEPES-Saline solution. These materials arrive purified by density gradient centrifugation. This solution was diluted into 5 mM MES, 5 mM HEPES, 5 mM citrate, 150 mM NaCl and 1 mM EDTA adjusted to pH 7.4 and then filtered using a Nalgene SFCA filter unit, 0.2  $\mu\text{m}$  pore size. A 1 M citric acid solution was also prepared. All solutions were made using water from a Barnstead 4-stage purifier, equipped with 5-nm spiral wound ultrafilter. Virus stock was maintained as received at  $-80^\circ\text{C}$  and solutions prepared just prior to measurement. Changes in pH were made by removing the samples from the light scattering instrument and adding an amount of citric acid solution sufficient to lower the pH to about 5.0. All solutions were filtered via syringe with 0.2  $\mu\text{m}$  Nalgene cellulose acetate filters. All buffers used for dilution were filtered through a 0.1  $\mu\text{m}$  Millex filter. Latex solutions (used in control experiments) were prepared using Bangs Laboratories (Fishers, IN)

0.165  $\mu\text{m}$  diameter latex microspheres and diluted to have similar scattering to that of the virus solution at full concentrations.

### 4.3.2 SLS/DLS Measurements

The SLS/DLS apparatus was built in house, and consisted of a Millennia II 532 nm laser (green), a copper sample cell with a filtered toluene bath and equipped with a thermal bath for temperature control. A Hamamatsu R955P photomultiplier tube was mounted on a rotating arm. A Pacific Instruments model AD 126 amplifier-discriminator fed the data to a computer with an ALV 5000 correlator and associated software installed. Custom software was written to rapidly view and analyze each of the many sequential runs of the time-resolved experiments. Apparent diffusion values were computed at finite angles according to  $D_{\text{app}} = \Gamma/q^2$  (21) using 3<sup>rd</sup> order cumulants fits to for the data before and well after acidification. Second order cumulants fits were used during the time-resolved experiments. The channels selected for the cumulants fit enabled the method to accurately estimate the initial portion of the correlation function, as judged by plots of the residuals between measured data and fitted trend. The very first channels were always discarded to eliminate the effects of photomultiplier afterpulsing and pulse pile-up in the electronics. Channels in the tail, where the noise becomes significant compared to the difference between the signal trend and the estimated baseline, were also ignored. The measured parameters are not very sensitive to the specifics of channel selection, but in a wide-ranging autocorrelator some selection is always required.

## 4.4 Results and Discussion

The two strains of influenza virus (X-31 and PR-8) both were found to behave similarly and **Figure 4.1** shows a typical autocorrelation function for X-31 virus at 10

$\mu\text{g/mL}$ ,  $\theta = 30^\circ$  and pH 7.4. In this semilogarithmic representation, a single diffuser with no contributions from internal motions would be expected to give a straight line. A line fitted through the initial portion (i.e., times less than about 1 ms) of the correlation function demonstrates that there is some curvature to the experimental data. There is no sharp break in the plot, which would indicate two well-separated decay modes. At pH 7.4, the nonexponentiality parameter  $\mu_2 / \bar{\Gamma}^2$  decreased from about 0.2 to about 0.05 with increasing scattering angle. This is the behavior expected of a weakly polydisperse sample in which the large, strongly scattering and slowly diffusing particles contribute relatively less signal at high angles, leaving only the scattering from the remaining portion of the distribution. A rising nonexponentiality parameter could have indicated large, uniform particles of aspheric shape, such that rotation contributes to the relaxation of the correlation function at high  $q$ . Large, soft particles which exhibit flexural modes can also exhibit this type of behavior.<sup>45</sup>

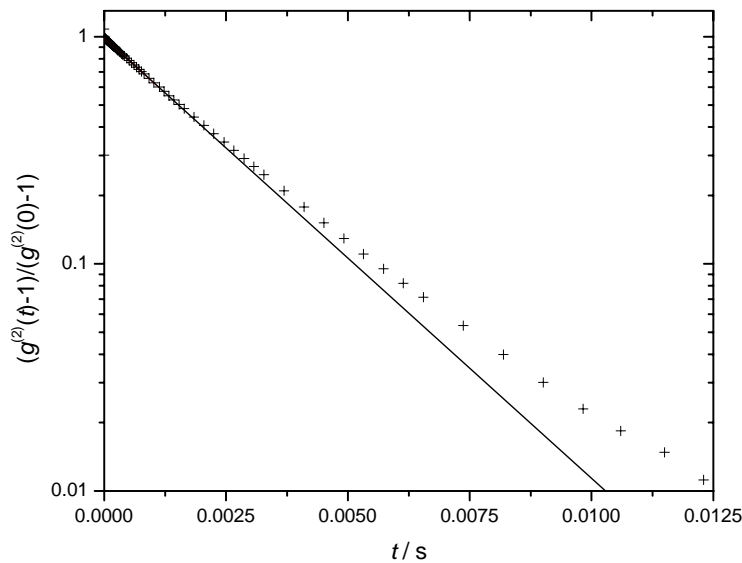


**Figure 4.1.** Intensity autocorrelation function for 10  $\mu\text{g/mL}$  X31 at  $\theta = 30^\circ$ .

**Figure 4.2** shows the trend of  $D_{\text{app}}$  with scattering vector magnitude. If the virus particles were monodisperse, small and spherical, **Figure 4.2** would exhibit no slope. The observed positive slope can arise from size polydispersity in a population containing large scatterers for the same reasons just outlined in discussing the  $\mu_2 / \bar{\Gamma}^2$  observations. A rising  $D_{\text{app}}$  vs  $q^2$  trend could also occur for monodisperse preparations if the particles are substantially aspheric and sufficiently large, but this is inconsistent with the observation that  $\mu_2 / \bar{\Gamma}^2$  decreased with angle at pH 7.4.

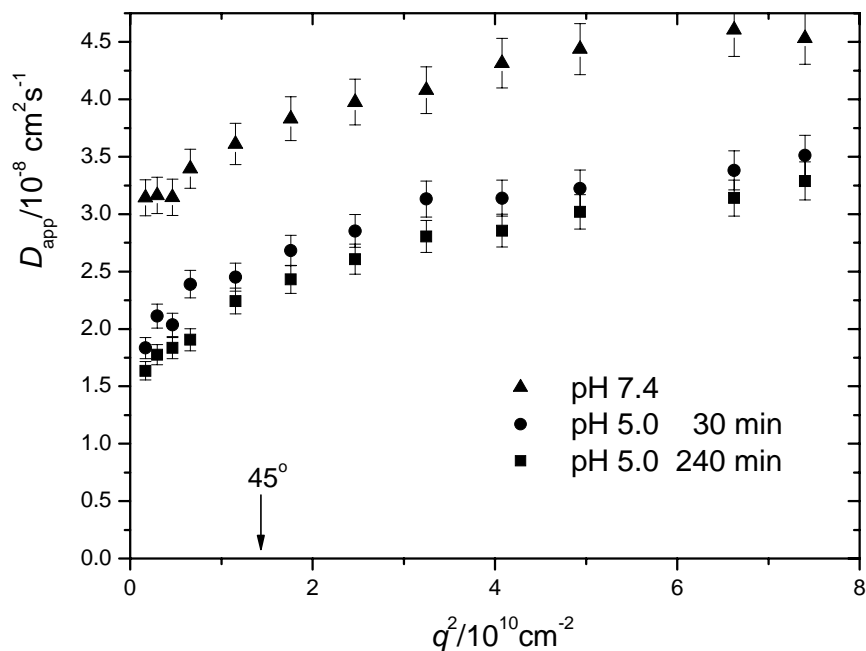


**Figure 2.** Apparent diffusion of PR-8 at 10  $\mu\text{g/mL}$  concentration and pH 7.4( $\blacktriangle$ ) and at 30( $\bullet$ ) and 240( $\blacksquare$ ) minutes after acidification to pH 5.0. Uncertainties are estimated as  $\sim \pm 5\%$ .

Size heterogeneity is the most likely cause for a rising trend in **Figure 4.2** and a decrease of  $\mu_2 / \bar{\Gamma}^2$  with scattering angle. Possible contributors to nonuniformity include

natural variability in size as the virus particles bud from a host cell, incomplete dissociation of aggregates upon dilution and breakage, but it is emphasized that the preparations are more uniform than many synthetic colloidal suspensions. The sizes corresponding to **Figure 4.2** are a little larger than often reported in electron microscopy studies. It is common for soft particles to shrink slightly during preparation for EM, while scattering methods tend to emphasize the higher moments of any given distribution. To gauge the latter effect, and even though Laplace inversion methods were generally not warranted, the program CONTIN was applied to the data of **Figure 4.1**. As expected from the modest and smooth curvature of that figure, the program returned a single peak, shown in **Figure 4.3**, centered at  $R_h \approx 980 \text{ \AA}$ . That number reflects scattering weighting—i.e., amplitude  $A_i \sim c_i M_i P_i(q)$ . The peak shifts to about  $810 \text{ \AA}$  for number weighting—i.e.,  $N_i \sim A_i / M_i^2 P_i(q)$  where it was assumed that  $M_i \sim R_{h,i}^3$  and  $P_i(q)$  was estimated assuming the sphere shape factor given in Eq. 10 below. The width of the distribution and the amount of the shift are overestimated because CONTIN introduces some width of its own.

PR-8 and X-31 both exhibit similar behavior upon lowering pH. As shown in **Figure 4.2** for PR-8, the apparent diffusion of the virus has declined after 30 minutes at pH 5 and further declines after 240 minutes. The rising  $D_{\text{app}}$  vs.  $q^2$  trend seen at pH 7.4 remains. The  $\mu_2 / \bar{\Gamma}^2$  nonexponentiality parameter was slightly higher than at pH 7.4. Though still modest at about 0.15-0.2, it no longer decreased with scattering angle. These observations are consistent with limited aggregation to produce a more heterogeneous distribution of larger, slightly more aspheric clusters. Size variation of substantially spherical objects would cause  $\mu_2 / \bar{\Gamma}^2$  to decrease with scattering angle, as it

did for virus at pH 7.4, but this effect may be offset by the appearance of rotational terms from the larger clusters, since the measurements are made at vectors as high as  $qR \sim 2.5$ .

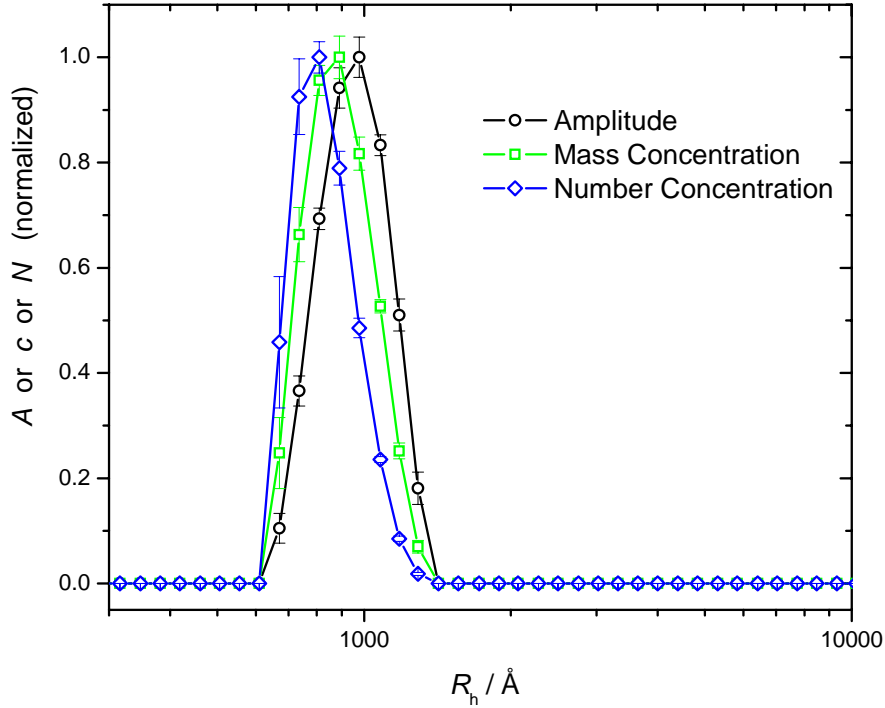


**Figure 4.3.** Radius distribution of X-31 at pH 7.4,  $T = 37^\circ\text{C}$ , estimated by CONTIN analysis of DLS data taken at  $\theta = 30^\circ$ . Circles: scattering amplitude,  $A$ . Squares: relative concentration,  $c$ . Circles: relative numbers,  $N$ . The distribution width, and the shift in peak location from  $A$  to  $c$  to  $N$ , is overestimated; see text. The error bars are those estimated by CONTIN (propagated for the  $c$  and  $N$  distributions).

We have avoided inverse Laplace transformation method<sup>48,49</sup> to characterize the decay rate distribution because they would not be effective for such small deviations from exponential behavior. The diffusion coefficient does decrease when spheres join aggregates, causing nonexponentiality, but the effect is not linear. For example, the diffusion coefficient of a dimer is 75% that of a single sphere.<sup>50-52</sup> The aggregation of

particles of unquestioned sphericity and uniformity to produce such a small difference might be worth pursuing by discrete two- or three-exponential analysis, but the smooth curvature of **Figure 4.1** and the  $\mu_2 / \bar{\Gamma}^2$  values seen prior to pH-induced aggregation discourage us from this type of analysis in the present case.

SLS proves more revealing than DLS for aggregates of such large size. The Guinier plot in **Figure 4.4** demonstrates how misleading measurements of intensity at a single scattering angle can be. At  $\theta = 90^\circ$ , often the only choice when one of the increasingly popular single angle instruments is used, there is not a significant change in intensity between the virus solution at pH 7.4 and the aggregated virus solution at pH 5.0. Measurements at low angles (down to  $15^\circ$ ) reveal a strong increase in the scattering power of the solutions.

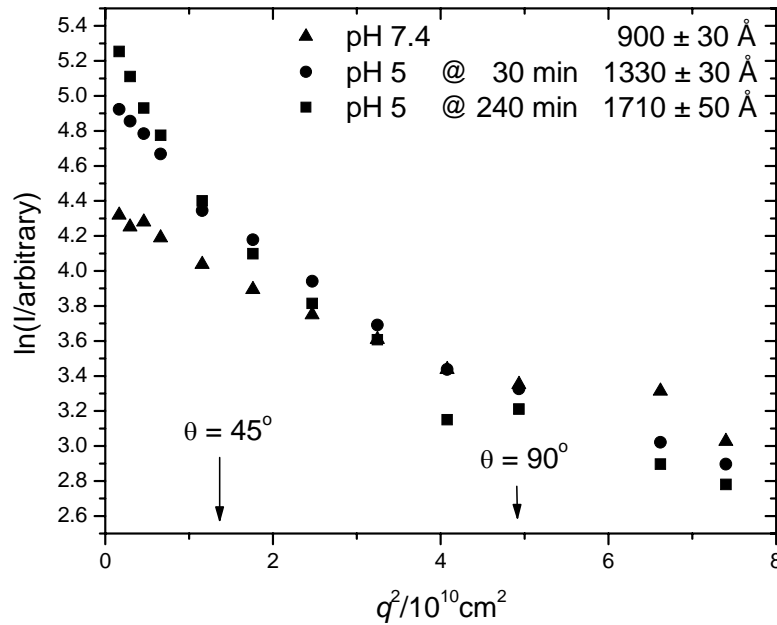


**Figure 4.4.** Guinier plots for PR-8 at 10 µg/mL; symbols as in Figure 2.

As described above, the intensity is proportional to the concentration and mass, reduced by the particle form factor.

$$I(q) = I_0 K_{\text{opt}} c M P(q) \quad (8)$$

An increase in  $I_0$  implies an increase in the mass of the particles or the optical constant,  $K_{\text{opt}}$ . The optical constant is proportional to the square of the specific refractive index increment, often called  $dn/dc$ <sup>50,53</sup>.

$$K_{\text{opt}} \sim (dn/dc)^2 \quad (9)$$

Attempts to measure either  $dn/dc$  or any change after acidification using a Brice-Phoenix apparatus or an even more sensitive Waters Model 410 were unsuccessful because of the low concentrations required to avoid turbidity. The required measurements would be very challenging on any differential refractometer. If  $K_{\text{opt}}$  were to fully account for the measured increase in scattering intensity after 240 minutes, which **Figure 4.4** shows to be about one power of the natural base,  $e$ ,  $dn/dc$  must rise by a factor of about  $e^{1/2} = 1.65$ . Such a large increase seems unlikely for the intact virus particle, although individual proteins undergo quite significant changes when fully denatured. Assuming no change in  $K_{\text{opt}}$ , aggregates containing  $e \cong 2.7$  particles, on average, can account for the rise in  $I_0$ . Thus, the intercept suggests a suspension of heterogeneous aggregates whose scattering is dominated by trimers after 240 minutes at pH 5. The increase in  $I_0$  after 30 minutes is about a factor of 2, suggesting that dimers are the average scattering particles. These results are only qualitative, but it proves interesting to test them for consistency with the angular dependence of the scattered intensity.

Analysis of the low- $q$ , linear regions of the plots in **Figure 4.4** shows that  $R_g$  rises from  $\sim 900 \text{ \AA}$  at pH 7.4 to  $\sim 1700 \text{ \AA}$  after 240 minutes at pH 5. This result does not depend on the shape of the scatterers. It is instructive to try to fit the measured scattering envelopes over their full range of  $q$  using the form factor for a solid sphere of radius,  $R$ , and aggregates of such spheres. The form factor of a single sphere is given by<sup>54</sup>

$$P_1(q) = \left[ \frac{3}{x^3} (\sin x - x \cos x) \right]^2 \quad (10)$$

where  $x = qR$ . Nonlinear fits are easily accomplished by an iterative search for  $I_0$  and  $R$  values that minimize the sum of squared errors. Initial guesses were supplied by the values from the Guinier plots, but the fits were insensitive to the starting parameters within a few Angstroms. Once  $I_0$  is found, both fitted curve and original data may be normalized for display purposes. Fits based on Eq. 10 were never completely satisfactory, but the results for pH 7.4 deserve mention as a basis for comparison; see **Figure 4.5a**. The apparent sphere radius of  $1000 \pm 30 \text{ \AA}$  exceeds the radius of gyration,  $R_g = 900 \pm 30 \text{ \AA}$  from the Guinier plot, but if the virus particles were uniformly solid and monodisperse spheres with  $R_g = 900 \text{ \AA}$ , one would expect<sup>50</sup> an even larger result,  $R = 1160 \text{ \AA}$  (i.e.,  $900 \times \sqrt{5/3}$ ). The fitted curve lies below the data at high  $q$  and, if anything, exceeds it slightly at intermediate  $q$ . One may conclude that the virus particles are not uniformly sized, solid spheres. These characteristics are exacerbated by acidification. No form factor for a single sphere, regardless of its size, even comes close to matching the data obtained after 240 minutes at pH 5. Multiple sphere form factors do.

The scattering from an  $N$ -particle, freely-rotating aggregate, normalized to that at  $q = 0$ , can be computed<sup>52</sup> as the product of the form factor for the individual particle and a structure factor,  $S(q)$ , that reflects the interparticle distances,  $r_{ij}$ :

$$P_N = P_1 S(q) \quad (11)$$

$$S(q) = \frac{1}{N^2} \sum_{i,j} \frac{\sin qr_{ij}}{qr_{ij}} \quad (12)$$

For example, the normalized scattering intensity for a linear trimer made of touching spheres is:

$$P_3(q) = \frac{P_1(q)}{9} \left[ 3 + 4 \cdot \frac{\sin(2qR)}{2qR} + 2 \cdot \frac{\sin(4qR)}{4qR} \right] \quad (13)$$

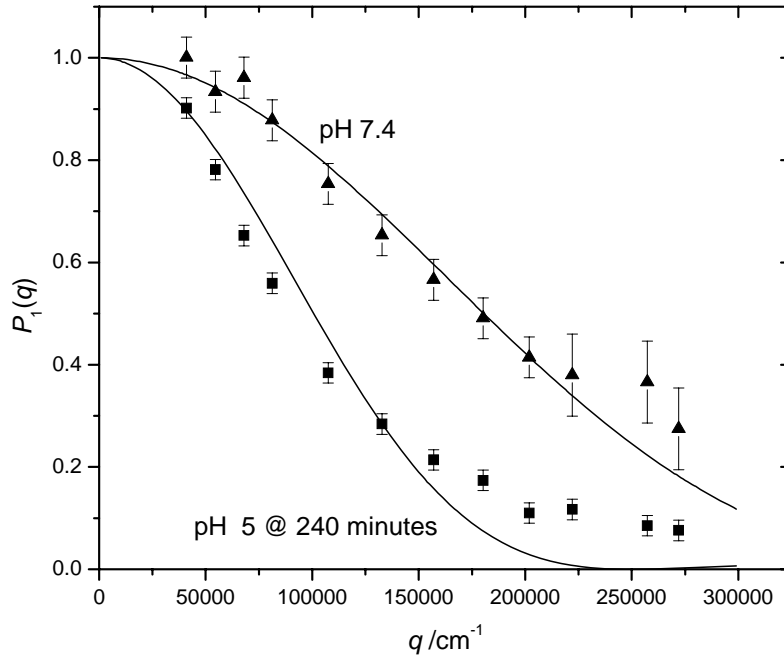


**Figure 4.5a.** Single-sphere fits (smooth curves, see Eq. 10) are not satisfying for virus particles at any measured condition, but come much closer at pH 7.4 than at lower pH. Same data and symbols as Figure 2.

**Figure 4.5b** overlays simulations for a linear dimer and a 50:50 mixture of linear and trigonal trimers onto the experimental data after 30 and 240 minutes at pH 5.0, respectively. The calculations were made with  $R = 1000\text{\AA}$ , the value obtained from the single sphere fit to the scattering profile at pH 7.4. The results are more satisfying than a fit to a single sphere model, regardless of size, but the scattering at high  $q$  still exceeds that expected from these simple models based on uniform, solid spheres.

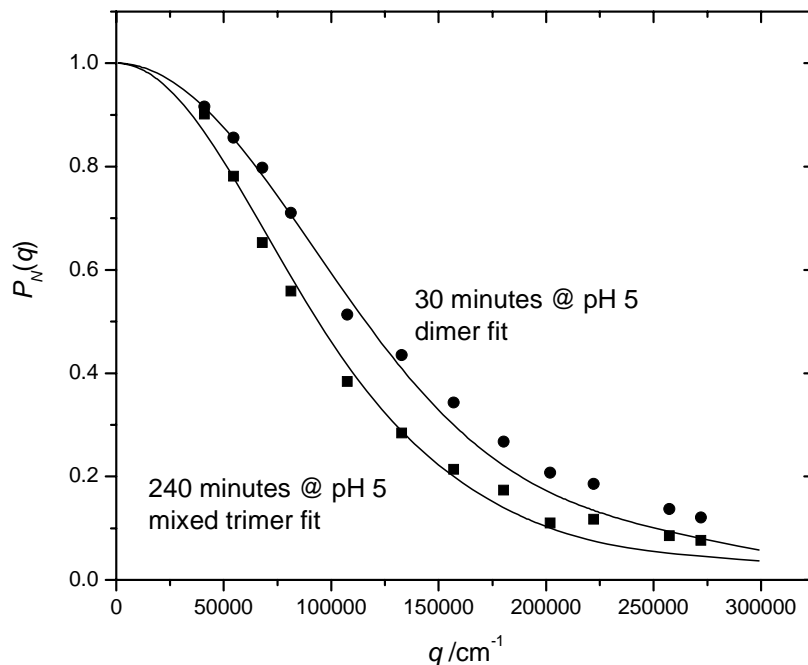


**Figure 4.5b.** A fit for a dimer of solid spheres,  $R = 1000\text{\AA}$ , is overlaid on data for PR-8 after 30 minutes at pH 5. The fit for a 50:50 mixture of linear and trigonal trimers is overlaid on the data for PR-8 after 240 minutes at pH 5. Same data and symbols as Figure 2. No claim is made about the uniqueness of these fits; they merely suggest that low levels of aggregation have occurred.

No attempt was made to optimize the fits by using ratios other than 50:50 linear:trimer, trying mixtures of monomers, dimers, trimers and tetramers in the various possible arrangements, etc. A unique fit would surely prove elusive, but the scattering envelopes

and all other data so far are consistent with limited aggregation of approximately spherical, polydisperse virus particles (and possible limited clusters of them) over a period of minutes to hours.

Time-resolved measurements reveal interesting details about the early pathway to aggregation, but we are only able to study both SLS and DLS simultaneously at one scattering angle. It should be low enough to permit at least some of the long-time intensity increase (**Figure 4.4**) to be observed, but choosing too low an angle will require long DLS acquisitions for the measurement of  $R_h$  (according to Eq. 2, the decay time increases at low scattering angles, and with it the time required to estimate the correlation function accurately). A scattering angle of  $\theta = 45^\circ$  was selected. An estimate of the error in hydrodynamic size, inversely proportional to diffusion coefficient, at this angle can be made by referring to **Figure 4.2**. Choosing the pH 7.4 data (it doesn't matter much which data set is used) the error estimate by inspection is  $100 \times (1/3.7 - 1/3.0)/(1/3.0) = 19\%$ . This is acceptable for the purpose of following  $R_h$  with time. Considerably greater error is incurred when following the intensity at  $\theta = 45^\circ$ ; the intensity trends below are qualitative only.

**Figures 4.6 and 4.7** show the evolution of scattered intensity and apparent hydrodynamic radius measured at  $\theta = 45^\circ$ , for the highest studied concentrations of PR-8 and X-31, respectively. The vertical scales have been selected to convey the overall magnitude of the transitions in a consistent fashion from one experiment to the next. The still-evident noise can be attributed to the short acquisition times used to estimate the correlation functions, this compromise being necessary to follow the changes with adequate time resolution. No importance should be attached to the absolute values of the

intensities, only to relative changes thereof. The X-31 strain is significantly larger than the PR-8, but for both virus strains,  $R_h$  rises suddenly after lowering the pH, and this is followed by gradual growth of  $R_h$  and intensity. The sudden increase in radius suggests a conformational change in the individual virus particles.

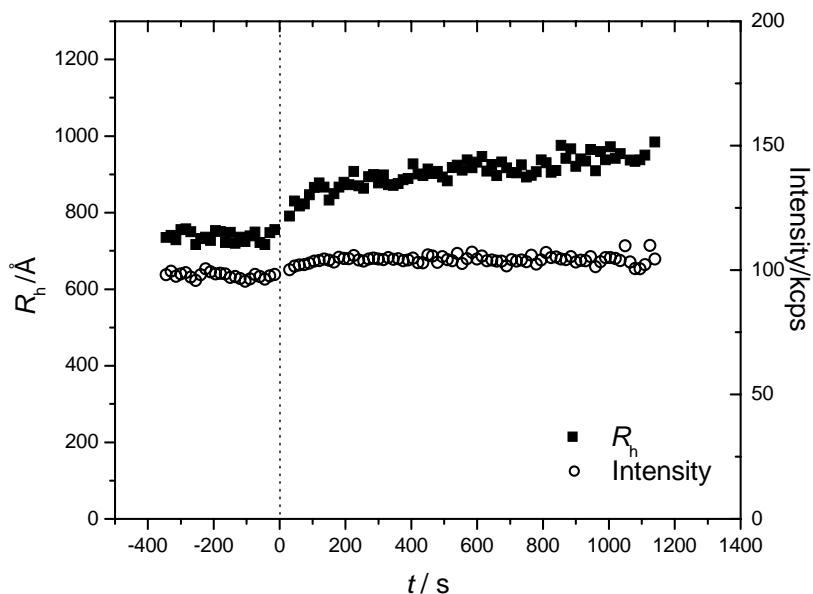


**Figure 4.6.** 10  $\mu\text{g}/\text{mL}$  solution of PR-8, time-resolved measurement at  $\theta = 45^\circ$ . Addition of citric acid for pH change is indicated by the vertical, dashed line at time 0.

This conformational change likely exposes the hydrophobic fusion peptide at the amino terminus of HA2, resulting in the slow aggregation of virus particles, perhaps in part as a consequence of fusion of one viral envelope with another. The rate of virus inactivation has been reported to be very much more rapid for PR-8 than for X-31.<sup>55</sup> Differences between the curve shapes of **Figures 4.6 and 4.7** are evident, but interpretation is not straightforward because the values of  $R_h$  and, especially, intensity at long times after pH adjustment are both underestimated at the single angle used. For

example, no significance can be attached to the leveling of intensity in **Figure 4.6**, even though  $R_h$  continues to grow. In **Figure 4.7**, the growth of intensity seems to track  $R_h$ , but again this does not represent the true scattering power of the solutions, as would be measured at zero angle.

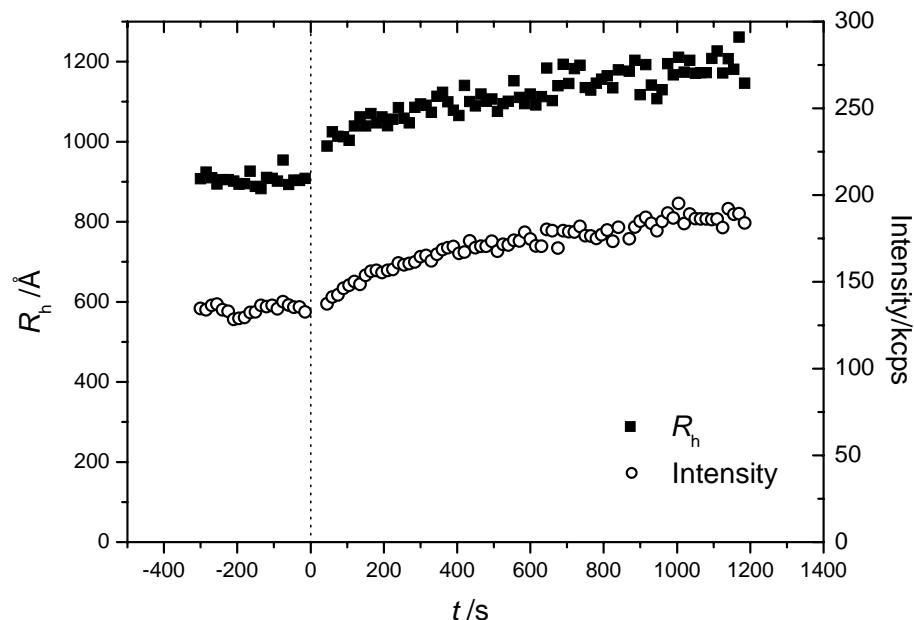


**Figure 4.7.** A 10  $\mu\text{g/mL}$  solution of X-31, time-resolved measurement at  $\theta = 45^\circ$ . Addition of citric acid for pH change is shown by the line at time 0.

In an attempt to separate the effects of conformational change from those due to aggregation, the concentration of the starting solution was reduced. **Figures 4.8 and 4.9** show time-resolved measurements at progressively lower virus concentrations. The initial radius for the lowest concentration in **Figure 4.9** is slightly (about 6%) lower than it was at the higher concentrations of **Figure 4.7** and 4.8. Perhaps aggregation is diminished slightly at the lowest concentration. Acidification always produces a sudden

change in  $R_h$  followed soon after by a slightly more gradual rise in  $R_h$  and scattered intensity, both underestimated because of the finite angle.

In **Figures 4.8 and 4.9**, the intensity is slightly reduced immediately after addition of the citric acid. This probably results from an unimportant artifact that, nevertheless, requires explanation.

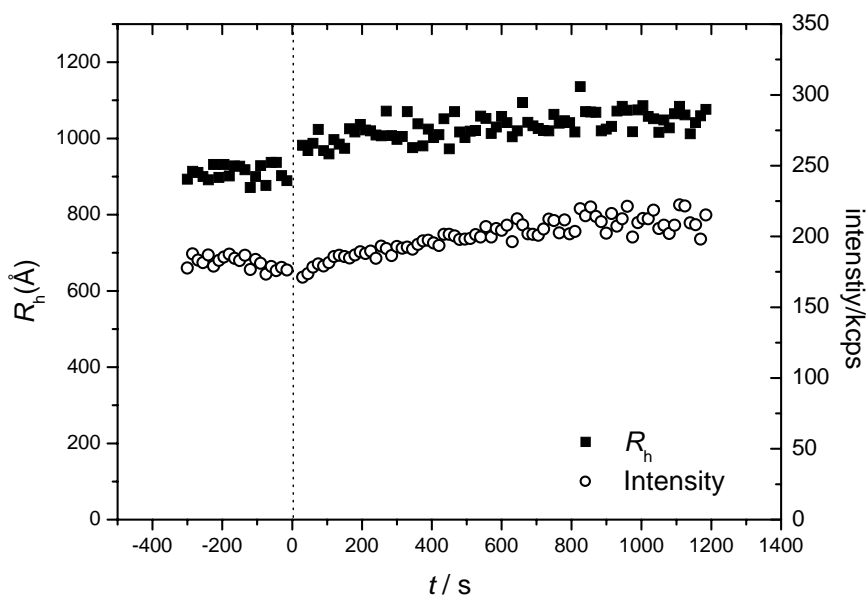


**Figure 4.8.** Same as Figure 4.7, but 5  $\mu\text{g/mL}$ .

In a conventional DLS instrument, light reaches the detector through a small (typically 100  $\mu\text{m}$ ) pinhole aimed at a focused laser beam of similar diameter. Due to undulations or small scratches, the vertical position of the beam can shift a small amount after removal of the sample and reinsertion after addition of citrate. When measuring a stationary sample, it is easy to recapture the exact vertical alignment, but the systems under study evolve so rapidly we elected to accept the tiny vertical shift. This has

absolutely no influence on measurement of  $R_h$ , and it does not affect the *trend* of the intensity following reinsertion.

The results tend to support the idea of a sudden change in conformation with a corresponding jump in the hydrodynamic radius of the intact virus particle by about  $100\text{\AA}$ , which is the magnitude of the change expected from the diffraction measurements<sup>56</sup> on the isolated HA ectodomain and from the formation of an extended coiled-coil structure.<sup>57</sup>

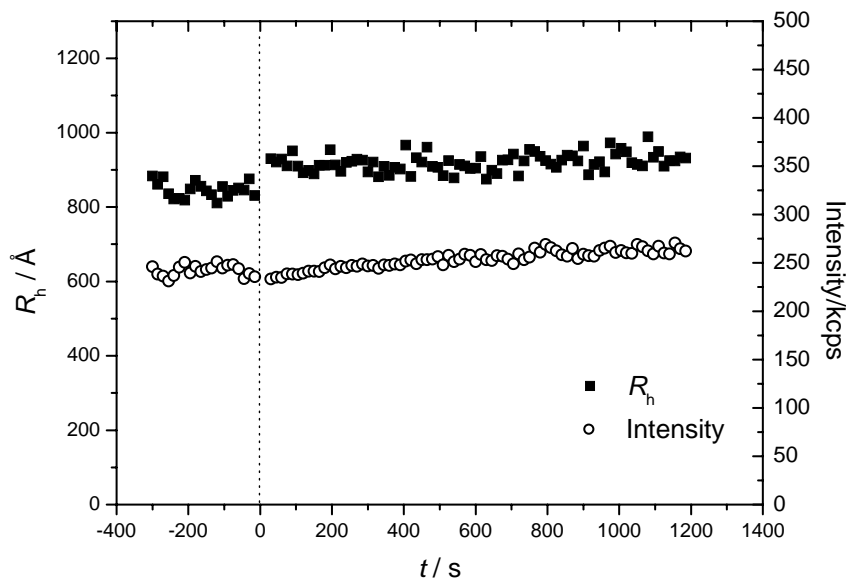


**Figure 4.9.** Same as Figure 4.7, but  $2\ \mu\text{g/mL}$ .

This conformational change is then likely followed by aggregation when the virus concentration is sufficiently high. At the still lower virus concentration of  $0.5\ \mu\text{g/mL}$ , both the initial jump and the subsequent intensification seemed absent or greatly retarded (not shown). This intriguing detail warrants further study if interference from dust,

impurities and undissolved aggregates can be eliminated in solutions of such low overall scattering power.

For comparative purposes, **Figures 4.10 and 4.11** show time-resolved measurements for polystyrene latex particles. These charge-stabilized particles also aggregate after the addition of citric acid (**Figure 4.10**) as indicated by the increase in scattering power. The latex does not show any sudden, initial change in size. Unlike virus particles, conformational change is not possible (the temperature was well below the glass transition temperature of polystyrene).

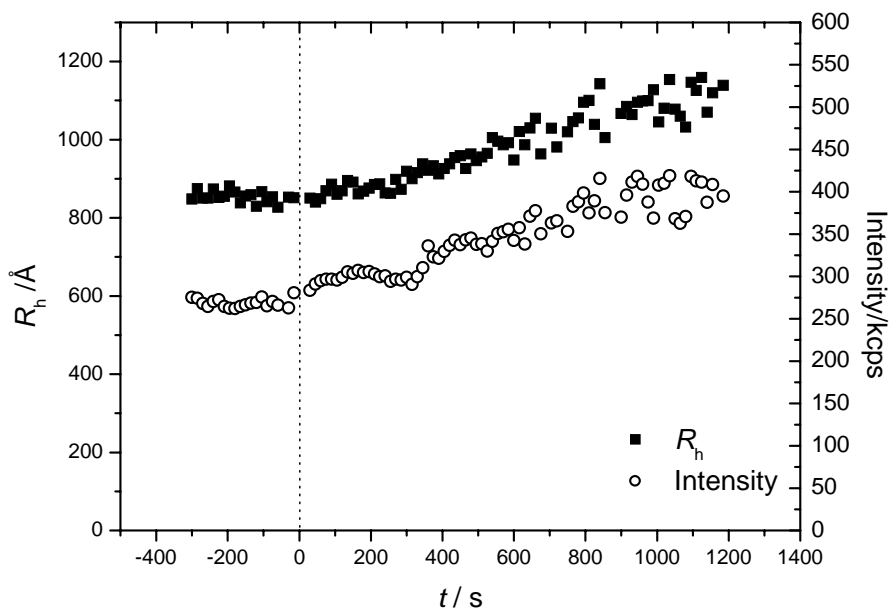


**Figure 4.10.** Latex particles in water and the addition of citric acid at time 0.

As a control, **Figure 4.11** shows a latex particle with the addition of water instead of citric acid. No effects are evident in  $R_h$ , and in this case the removal and reinsertion resulted in no vertical shift to affect the intensity.

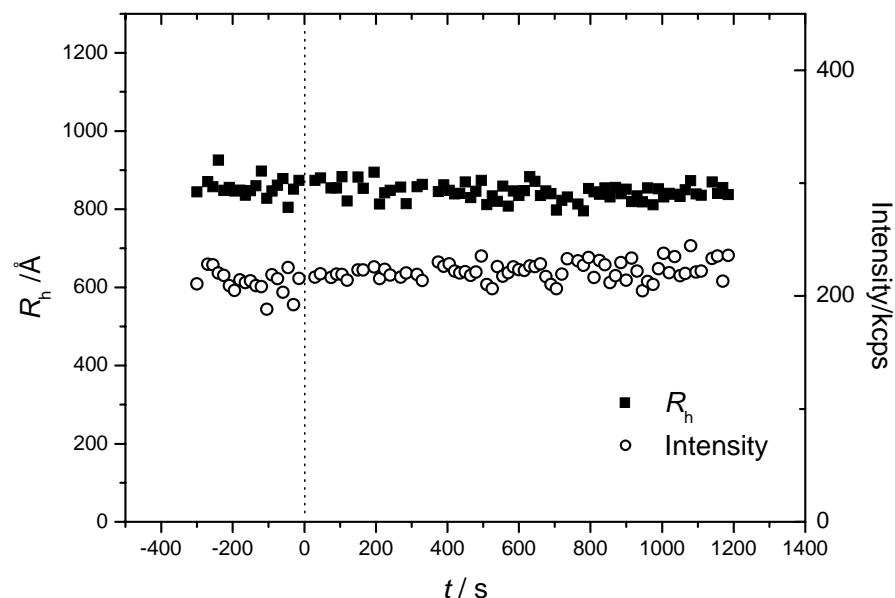


**Figure 4.11.** Latex after the addition of water at time 0.

## 4.5 Conclusion

Suspended at physiological pH, influenza virus particles are nonuniform with respect to size and are possibly aggregated slightly. This confirms, under very gentle conditions with no sample processing, the observations from electron microscopy. Upon acidification to pH 5, the particles aggregate over an extended period time. The data support the formation of low aggregates of the particles that existed at pH 7.4. Time-resolved measurements show, for the first time in intact virus particles, that aggregation is preceded by a rapid conformational change involving an expansion of about 100 Å in hydrodynamic radius. This is in agreement with studies on isolated HA components. Even for intact virus, the conformational change is essentially instantaneous on the time scale of the present measurements. One may look to small angle X-ray or small angle

neutron scattering measurements for short range structural details,<sup>42</sup> but these methods are not well suited to following rapid changes.

There are some common elements in several of the recently proposed mechanisms of influenza fusion.<sup>58-62</sup> All of these pathways include the formation of an extended coiled-coil that would increase the length of the HA protein. Electron microscopy studies and measurement of the hydrodynamic radius by sedimentation velocity indicates that the length of the isolated ectodomain of HA increases by  $\sim 50$  Å.<sup>37</sup> This estimate is in reasonable agreement with our estimate of 100 Å by light scattering. It is possible that the change in length of the ectodomain is an underestimate, if there is overlap of the individual proteins in the aggregates. These changes are larger than previous estimates by electron microscopy of the intact virus.<sup>43,44</sup> It is possible that freezing results in some distortions in the specimens used for microscopy or that the method is not of sufficiently high resolution to detect a thin extension of protein. This change in conformation resulting from acidification is suggested to be coupled to insertion of the fusion peptide, located at the end of the stalk, into the target membrane. However, there are also suggestions that the fusion peptide first inserts into the viral membrane. Our results indicate that if this occurred, it must be an extremely rapid, transient event. In addition, the fact that the protein can extend from the virus without the presence of a target membrane indicates that insertion of the fusion peptide into the target is not the energetic driving force for this conformational rearrangement. At other stages of the fusion process, the extended coiled-coil changes its juxtaposition with regard to the membrane from one in which its long axis extends orthogonally from the membrane interface to one in which the spike lies along the plane of the membrane at the interface. Our findings

indicate that in the absence of a target membrane, this rearrangement does not occur. Our results describe what occurs in a native intact virus, in which the surface density of viral proteins is very high. The situation may not correspond to a transfected cell that can have a much lower content of HA in the plasma membrane.

Future studies of the aggregation of influenza virus or similarly sized colloidal particles may benefit from simultaneous, time-resolved, multi-angle SLS and DLS measurements using multiple correlators. Extrapolating the intensity,  $R_g$  and  $R_h$  results to  $q = 0$  would result in more revealing kinetic trends. If the true increase in scattering power (related to mass, assuming  $dn/dc$  remains constant) can be separated from size changes, that will reveal something of the particle shape and changes thereto. Suitably extrapolated to  $q = 0$ , the quotient  $R_g/R_h$  can also reveal information about shape change. A number of interesting problems await such instrumentation. In the case of influenza virus, these include the reversibility of pH-induced changes, behavior upon acidification to other pH values, and the effects of added salt.

## References

- 1) T. Ward. *Anal. Chem.* **2000.** 72. 4521.
- 2) W. Pirkle. T. Pochapsky. *Chem. Rev.* **1989.** 89, 347.
- 3) L. Salam; X. Chapuisat; G. Segal; P. Hiberty; C. Minot; C. Leforrestier; P. Sautet. *J. Am. Chem. Soc.* **1987.** 109, 2887.
- 4) G. Ogsten. *Nature* **1948.** 162, 963
- 5) G. Wulff; A. Sarhan; K. Zabrocki *Tetrahedron Letters* **1973,** 44, 4329.
- 6) G. Wulff; W. Vesper; A. Sarhan; R. Grobe-Einsler *Makromol. Chem.* **1977,** 178, 2799.
- 7) M. Kempe; K. Mosbach *J. Chromatography.* **1990.** 516(2), 313.
- 8) G. Wulff. *Chem Rev.* **2002.** 102, 1.
- 9) B. Sellegren. *J. Chromatography A.* **2001.** 906, 227.
- 10) G. Wulff. *Angew. Chem., Int. Ed.* **1995.** 34, 1812
- 11) V. P. Joshi, M. G. Kulkarni, and R. A. Mashelkar. *J. Chromatogr. A.* **1999.** 849, 319.
- 12) E. O. Dela Cruz, H. Muguruma, W.I. Jose, and H. Pederson. *Anal. Lett.* **1999.** 32, 841.
- 13) T. P. O'brian, N. H. Snow, N. Grinberg, and L. Crocker. *J. Liq. Chromatogr. Relat. Technol.* **1999.** 22, 183.
- 14) L. I. Andersson, D. J. O'shannessy and K. Mosbach. *J. Chromatogr.* **1990.** 513, 167.
- 15) G. Wulff. *ACS Symp. Ser.* **1986.** 308, 186.
- 16) Z. H. Meng, L. M. Hou, Q. H. Wang, and D. Q. Zhu, *Chin. Chem. Lett.,* **1997.** 8, 354.
- 17) D. Spivak, J. Campbell. *Analyst.* **2001.** 126, 793
- 18) E. Juaristi, P. Murer, D. Seebach, *Synthesis.* **1993.** 1243-1246.
- 19) A. Abdel-Magid, K.G. Carson, B. Harris, C.A. Maryanoff, R.D. Shah, *J. Org. Chem.* 61 **1996.** 3849-3862.

- 20) H. Rezaei, I. Marek, J. Normant, *Tetrahedron* **57**. **2001**. 2477-2483.
- 21) P. Beak, A. Basha, B. Kokko, D. Loo, *J. Am. Chem. Soc.* **108** **1986**. 6016-6023.
- 22) A. Corruble, J. Valnot, J. Maddaluno, P.J. Duhamel, *Org. Chem.* **63** **1998**. 8266-8275.
- 23) B. Ranu, A. Majee, A.I. Sarkar, *J. Org. Chem.* **63** **1998**. 370-373.
- 24) L.I. Andersson, D.J. O'Shannessy, K. Mosbach, *J. Chromatogr.* **513** **1990**. 513, 167-179.
- 25) D.A. Spivak, K.J. Shea, *J. Am. Chem. Soc.* **119** **1997**. 4388-4393.
- 26) Cox, N. J.; Tamblyn, S. E.; Tam, T. *Vaccine* **2003**. 21(16), 1801-1803.
- 27) Ruigrok, R. W.; Krijgsman, P. C.; Ronde-Verloop, F. M.; de Jong, J. C. *Virus Res.* **1985**. 3(1), 69-76.
- 28) Wrigley, N. G.; Skehel, J. J.; Charlwood, P. A.; Brand, C. M. *Virology* **1973**. 51(2), 525-529.
- 29) Oxford, J. S.; Corcoran, T.; Hugentobler, A. L. *J.Biol.Stand.* **1981**. 9(4), 483-491.
- 30) Jin, H.; Leser, G. P.; Zhang, J.; Lamb, R. A. *EMBO Journal* **1997**. 16(6), 1236-1247.
- 31) Han, X.; Tamm, L. K. *J.Mol.Biol.* **2000**. 304 953-965.
- 32) Korte, Th.; Ludwig, K.; Krumbiegel, M.; Zirwer, D.; Damaschun, A.; Herrmann, A. *Journal of Biological Chemistry* **1996**. 272 9764-9770.
- 33) Blumenthal, R.; Clague, M. J.; Durell, S. R.; Epanand, R. M. *Chemical Reviews* **2003**. 103(1), 53-69.
- 34) Bullough, P. A.; Hughson, F. M.; Skehel, J. J.; Wiley, D. C. *Nature* **1994**. 371(6492), 37-43.
- 35) Chen, J.; Skehel, J. J.; Wiley, D. C. *Proc.Natl.Acad.Sci.U.S.A* **1999**. 96(16), 8967-8972.
- 36) Wilson, I. A.; Skehel, J. J.; Wiley, D. C. *Nature* **1981**. 289(5796), 366-373.
- 37) Ruigrok, R. W.; Wrigley, N. G.; Calder, L. J.; Cusack, S.; Wharton, S. A.; Brown, E. B.; Skehel, J. J. *EMBO Journal* **1986**. 5(1), 41-49.
- 38) Bottcher, C.; Ludwig, K.; Herrmann, A.; van Heel, M.; Stark, H. *FEBS Lett.* **1999**. 463(3), 255-259.

- 39) Gruenke, J. A.; Armstrong, R. T.; Newcomb, W. W.; Brown, J. C.; White, J. M. *Journal of Virology* **2002**. 76(9), 4456-4466.
- 40) Ruigrok, R. W.; Aitken, A.; Calder, L. J.; Martin, S. R.; Skehel, J. J.; Wharton, S. A.; Weis, W.; Wiley, D. C. *J.Gen.Virol.* **1988**. 69 ( Pt 11) 2785-2795.
- 41) Booy, F. P.; Ruigrok, R. W.; van Bruggen, E. F. *Journal of Molecular Biology* **1985**. 184(4), 667-676.
- 42) Cusack, S.; Ruigrok, R. W.; Krygsmann, P. C.; Mellema, J. E. *Journal of Molecular Biology* **1985**. 186(3), 565-582.
- 43) Kanaseki, T.; Kawasaki, K.; Murata, M.; Ikeuchi, Y.; Ohnishi, S. *J.Cell Biol.* **1997**. 137(5), 1041-1056.
- 44) Shangguan, T.; Siegel, D. P.; Lear, J. D.; Axelsen, P. H.; Alford, D.; Bentz, J. *Biophysical Journal* **1998**. 74(1), 54-62.
- 45) Berne, B.; Pecora, R. *Dynamic Light Scattering*; Wiley: New York, **1976**.
- 46) Chu, B. *Laser Light Scattering*; 2 ed.; Academic Press: New York, **1991**.
- 47) Koppel, D. E. *J.Chem.Phys.* **1972**. 57 4814-4820.
- 48) Provencher, S. W. *Comp.Phys.* **1982**. 27 213-227.
- 49) Provencher, S. W. *Comp.Phys.* **1982**. 27 229-242.
- 50) Tanford, C. *Physical Chemistry of Macromolecules*; John Wiley & Sons: New York, **1961**.
- 51) Riseman, J.; Kirkwood, J. G. *J.Chem.Phys.* **1950**. 18 512.
- 52) Bloomfield, V. A. *Biopolymers* **2000**. 54 168-172.
- 53) Van Holde, K. E. *Physical Biochemistry*; 2 ed.; Prentice-Hall, Inc.: Englewood Cliffs, N. J., **1985**.
- 54) Kratochvil, P. in *Light Scattering from Polymer Solutions*, Huglin, M. B., editor; Academic Press: New York, **1972**. Chapter 7, pp. 333-379.
- 55) Korte, T.; Ludwig, K.; Krumbiegel, M.; Zirwer, D.; Damaschun, G.; Herrmann, A. *Journal of Biological Chemistry* **1997**. 272(15), 9764-9770.

- 56) Weissenhorn, W.; Dessen, A.; Calder, L. J.; Harrison, S. C.; Skehel, J. J.; Wiley, D. C. *Mol.Membr.Biol.* **1999**. 16(1), 3-9.
- 57) Carr, C. M.; Kim, P. S. *Cell* **1993**. 73(4), 823-832.
- 58) Tamm, L. K. *Biochim.Biophys.Acta* **2003**. 1614(1), 14-23.
- 59) Park, H. E.; Gruenke, J. A.; White, J. M. *Nature Structural Biology* **2003**. 10(12), 1048-1053.
- 60) Borrego-Diaz, E.; Peeples, M. E.; Markosyan, R. M.; Melikyan, G. B.; Cohen, F. S. *Virology* **2003**. 316(2), 234-244.
- 61) Jardetzky, T. S.; Lamb, R. A. *Nature* **2004**. 427(6972), 307-308.
- 62) Bentz, J.; Mittal, A. *Biochim.Biophys.Acta* **2003**. 1614(1), 24-35.

## Appendix : Letters of Permission

Reproduced in part with permission from Systematic Study of Steric and Spatial Contributions to Molecular Recognition by Non-Covalent Imprinted Polymers. Spivak, David A.; Campbell, Jason. *Analyst* (2001), 126 (6), 793-797. Copyright 2001 Royal Chemical Society.

Reproduced in part with permission from Evidence for Shape Selectivity in Non-Covalent Imprinted Polymers. Spivak, David A.; Simon, Ryan; Campbell, Jason. *Analytica Chimica Acta* (2004), 504(1), 23-30. Copyright 2004. Elsevier Science Limited.

Reproduced in part with permission from Structural Changes and Aggregation of Human Influenza Virus. Campbell, Jason N.; Epan, Richard; Russo, Paul S. *Biomacromolecules* (2004), 5, 1728-1735. Copyright 2004. American Chemical Society.



ELSEVIER

Mr Jason Campbell

[Jcampb6@lsu.edu](mailto:Jcampb6@lsu.edu)

Dear Mr Campbell

ANALYTICA CHIMICA ACTA, Vol 504, No 1, 2004, Pages 23-30, Spivak et al, 'Evidence for ...', Figures and some text only

As per your letter dated 8 August 2005, we hereby grant you permission to reprint the aforementioned material at no charge **in your thesis** subject to the following conditions:

1. If any part of the material to be used (for example, figures) has appeared in our publication with credit or acknowledgement to another source, permission must also be sought from that source. If such permission is not obtained then that material may not be included in your publication/copies.

2. Suitable acknowledgment to the source must be made, either as a footnote or in a reference list at the end of your publication, as follows:

“Reprinted from Publication title, Vol number, Author(s), Title of article, Pages No., Copyright (Year), with permission from Elsevier”.

3. Reproduction of this material is confined to the purpose for which permission is hereby given.

4. This permission is granted for non-exclusive world **English** rights only. For other languages please reapply separately for each one required. Permission excludes use in an electronic form. Should you have a specific electronic project in mind please reapply for permission.

5. This includes permission for UMI to supply single copies, on demand, of the complete thesis. Should your thesis be published commercially, please reapply for permission.

Yours sincerely

Helen Gainford  
Rights Manager

Dear Dr Campbell

The Royal Society of Chemistry (RSC) hereby grants permission for the use of your paper(s) specified below in the printed or microfilm version of your thesis. You may also make available the PDF version of your

paper(s) that the RSC sent to the corresponding author(s) of your paper(s) upon publication of the paper(s) in the following ways: in your thesis via any restricted internal website that your university may have for the deposition of theses, via your university's Intranet or via your own personal website. The Royal Society of Chemistry is a signatory to the STM Guidelines on Permissions (available on request).

Please note that if the material specified below or any part of it appears with credit or acknowledgement to a third party then you must also secure permission from that third party before reproducing that material.

Please ensure that the published article states the following:

Reproduced by permission of The Royal Society of Chemistry

Regards

Alice Chapman  
Contracts & Copyright Executive

## Vita

Jason Campbell was born in Bossier City, Louisiana, and attended high school at Airline High school in Bossier City. He received his Bachelor of Science degree in biochemistry from Louisiana State University in Shreveport in 1998. He was married to his wife Michelle in October of 2003, and had a daughter Kathleen in July of 2005. His plans after graduation are to work for Brookwood Pharmaceuticals in Birmingham, Alabama.